Monthly Notices
of the
ROYAL ASTRONOMICAL SOCIETY

MNRAS **479,** 4907–4935 (2018)
Advance Access publication 2018 June 26

doi:10.1093/mnras/sty1676

Starburst–AGN mixing: TYPHOON observations of NGC 1365, NGC 1068, and the effect of spatial resolution on the AGN fraction

Joshua J. D'Agostino,[1,2]★ Henry Poetrodjojo,[1,2] I-Ting Ho,[3] Brent Groves,[1,2] Lisa Kewley,[1,2] Barry F. Madore,[4] Jeff Rich[4] and Mark Seibert[4]

[1]*Research School of Astronomy and Astrophysics, The Australian National University, Cotter Road, Weston ACT 2611, Australia*
[2]*ARC Centre of Excellence for All Sky Astrophysics in 3 Dimensions (ASTRO 3D)*
[3]*Max Planck Institute for Astronomy, Königstuhl 17, D-69117 Heidelberg, Germany*
[4]*Observatories of the Carnegie Institution of Washington, 813 Santa Barbara St, Pasadena, CA 91101, USA*

Accepted 2018 June 22. Received 2018 June 22; in original form 2018 April 16

ABSTRACT

We demonstrate a robust method of resolving the star formation and AGN contributions to emission lines using two very well known AGN systems: NGC 1365 and NGC 1068, using the high spatial resolution data from the TYPHOON/PrISM survey. We expand the previous method of calculating the AGN fraction by using theoretical-based model grids rather than empirical points. The high spatial resolution of the TYPHOON/PrISM observations shows evidence of both star formation and AGN activity occurring in the nuclei of the two galaxies. We rebin the data to the lower resolutions, typically found in other integral field spectroscopy surveys such as SAMI, MaNGA, and CALIFA. The results show that when rebinned from the native resolution of TYPHOON (<200 pc pixel^{-1}) to 1 kpc pixel^{-1}, the effects include an ∼3 kpc increase in the radius of measured AGN activity, and a factor of 2–7 increase in the detection of low surface brightness features such as shocks. All of this information is critical, because information on certain physical processes may be lost at varying resolutions. We make recommendations for analysing data at current IFU survey resolutions.

Key words: galaxies: active – galaxies: evolution – galaxies: nuclei – galaxies: Seyfert – galaxies: starburst – galaxies: star formation.

1 INTRODUCTION

Much work has been undertaken to establish the relationship between the accretion activity of supermassive black holes (SBHs) and the evolution of their host galaxies (Cattaneo, Haehnelt & Rees 1999; Haehnelt & Kauffmann 2000; Cid Fernandes et al. 2001; Kauffmann et al. 2003; Granato et al. 2004; LaMassa et al. 2012). We now know that the mass of the SBH correlates with other properties of the galaxy, such as the velocity dispersion (M–σ relation; e.g. Ferrarese & Merritt 2000; Gebhardt et al. 2000; Tremaine et al. 2002; Gültekin et al. 2009; McConnell & Ma 2013), the stellar mass in the bulge ($M_{\rm BH}$–M_* relation; e.g. Magorrian et al. 1998; Marconi & Hunt 2003; Bennert et al. 2011; McConnell & Ma 2013), and the luminosity of the bulge ($M_{\rm BH}$–L; e.g. Marconi & Hunt 2003; Gültekin et al. 2009; McConnell & Ma 2013). Therefore, one might expect that black hole activity correlates with star formation. Yet, all current theories that link these processes, such as mergers, starburst-driven winds, or AGN-driven outflows (e.g. Yuan, Kewley & Sanders 2010a; Rafferty et al. 2011), have remained unconvincing. No theoretical model has successfully been able to explain the relationship between star formation and AGN (see the review by Alexander & Hickox 2012).

Emission lines such as Hα are one of the key measures for the growth of the stellar mass and SBH in galaxies across cosmic time. However, such lines can arise from both AGN and star-forming processes, making the determination of the relative rate of growths difficult when both are present. This confusion presents one of the difficulties in understanding the link between galaxy and SBH growth. Line ratio diagnostic diagrams, such as those suggested by Baldwin, Phillips & Terlevich (1981; commonly referred to as the 'BPT diagram'), Veilleux & Osterbrock (1987), Kewley et al. (2001), and Kewley et al. (2006), can be used to determine the dominant power source within a galaxy. The flux from hydrogen recombination lines such as Hα and Hβ is proportional to the number of ionizing photons emitted by a stellar cluster, which is proportional to the birth rate of massive stars (Dopita et al. 2002a, and references therein). Hence, the flux of Hα specifically (rather than Hβ which typically has a smaller flux due to the process that governs the two emission lines, as well as Hβ being more prone to

★ E-mail: joshua.dagostino@anu.edu.au

extinction and stellar absorption) is typically used as a star formation indicator. The [N II]λ6584 and [O III]λ5007 lines (hereafter simply [N II] and [O III] unless specified) are strong, forbidden lines and are easily measurable. These lines are AGN indicators because the extreme ultraviolet (EUV) radiation field from the accretion disc of the central AGN is harder than the radiation field from star formation (Groves, Dopita & Sutherland 2004; Kewley et al. 2006, 2013).

Work on starburst–AGN mixing was first explored by Kewley et al. (2001), using previous spectroscopy techniques. These previous spectroscopy techniques (e.g. long-slit) obtained a spectrum from a galaxy as a whole. As a result, galaxies were typically classified on the BPT diagram as either star forming or from an AGN, with the exception being when their line ratios placed them in the region of the BPT between the Kewley and Kauffmann demarcation lines (see Kewley et al. 2001; Kauffmann et al. 2003, respectively). These two lines are theoretical and empirical upper bounds of star formation in galaxies, respectively. The region between these two lines is interpreted to imply mixing of both star formation and an additional hard component (from e.g. AGN, shocks, or diffuse ionized gas) in galaxies (Yuan, Kewley & Sanders 2010b). Through their work with starburst galaxy modelling, Kewley et al. (2001) demonstrated with their SDSS sample that a continuum of ionizing sources (a 'mixing sequence') exists in galaxies. This notion was taken further by Kewley et al. (2006), who demonstrated that contributions from various ionizing sources could be calculated and extracted from galaxies which show multiple sources of ionization.

It is anticipated that the study of starburst–AGN mixing and uncovering the relationship between the two processes will become clearer with the advent of integral field spectroscopy (IFS). IFS, unlike previous methods, obtains spatially resolved spectra from individual spaxels across a galaxy, rather than a single spectrum that encompasses the galaxy as a whole. This allows both star formation and AGN processes in a single galaxy to be separated, and hence integral field unit (IFU) data is central to the study of starburst–AGN mixing. Starburst–AGN mixing using IFU data was first investigated by Davies et al. (2014a,b), who calculated the 'AGN fraction' for NCG 7130 from the Great Observatory All-Sky LIRG Survey (GOALS; Armus et al. 2009), and four galaxies (NGC 6394, NGC 2410, IC 0540, NGC 6762) from the Calar Alto Legacy Integral Field Area (CALIFA; Sánchez et al. 2012; Husemann et al. 2013). They make use of the concept of 'star-forming distance' defined in Kewley et al. (2006) to empirically fit each galaxy's mixing sequence from the star-forming to the AGN regions on the BPT diagram. We expand on the work conducted by Davies et al. (2014a,b) by calculating the AGN fraction with new theoretical models, rather than the Davies et al. (2014a,b) empirical method.

Using data obtained from the TYPHOON/Progressive Integral Step Method (PrISM) survey, we analyse two galaxies: NCG 1365 and NGC 1068, described in Section 2. TYPHOON/PrISM is a survey of 100 of the nearest and largest spiral galaxies, resulting in an incredibly highly resolved data set. The survey and data set are described further in Section 3. The high resolution of the data set gives a clean separation of both star formation and AGN processes in each galaxy, allowing very accurate calculations of the contribution to emission lines from both star formation and AGN processes. We calculate the AGN fraction for both NGC 1365 and NGC 1068 using new theoretical models. The models are described in Section 4, and the new AGN fraction calculation is showcased in Section 5. Further, we explore systematically the impact of resolution on determining the true contributions to both processes in Section 6 by rebinning the data to lower spatial resolutions and repeating the analysis.

2 SAMPLE SELECTION

2.1 NGC 1365

NGC 1365 is a large barred spiral galaxy [SB(s)b; de Vaucouleurs et al. 1991] located at a distance of roughly 18 Mpc in the constellation Fornax. NGC 1365 is roughly four times bigger than the Milky Way, with a semimajor axis of ∼32 kpc. NGC 1365 has a Seyfert 1.8 nucleus (Véron-Cetty & Véron 2006) with a rapidly rotating SBH of mass $M_{\rm BH} \approx 2 \times 10^6\,{\rm M}_\odot$ and spin parameter $a > 0.84$ (Reynolds 2013; Risaliti et al. 2013).

Large-scale outflows from NGC 1365 have been reported since the middle of the 20th century (for a detailed discussion on the history of reported outflows, see Veilleux et al. 2003, and references therein). Veilleux et al. (2003) confirm previous studies by measuring a biconical outflow south-east and north-west from the nucleus of NGC 1365. The opening angle of the biconical outflow has been suggested to be ∼100°, with a position angle of 126° (Hjelm & Lindblad 1996). Veilleux et al. (2003) and Sharp & Bland-Hawthorn (2010) also show high [N II]/Hα and [O III]/Hβ ratios particularly along the axis of the biconical outflow, up to values of 1.5 and 3 for each of the respective ratios (figs 6d and 7d, respectively, from Veilleux et al. 2003). The high emission line ratios suggest photoionization from the central AGN. The biconical outflow structure is roughly aligned with a radio jet-like feature at a position angle of 125°, observed in Sandqvist, Joersaeter & Lindblad (1995) and Morganti et al. (1999).

2.2 NGC 1068

As the prototypical Seyfert galaxy, NGC 1068 has been the subject of much work in the astronomical community, leading to it being arguably the most-studied active galaxy in the local Universe. A Seyfert 2 (Osterbrock & Martel 1993) (R)SA(rs)b (de Vaucouleurs et al. 1991) galaxy, it is located at a distance of roughly 12.5 Mpc in the constellation Cetus. The galaxy's broad-line region is known to be obscured by an optically thick torus (e.g. Miller & Antonucci 1983; Antonucci & Miller 1985; Miller, Goodrich & Mathews 1991; García-Burillo et al. 2016), and hence has largely been hidden from view due to extinction in the past (Rigby 2006). However, recent work such as Marinucci et al. (2016) and García-Burillo et al. (2016) has begun to resolve the nucleus and circumnuclear disc of NGC 1068.

NGC 1068 is also observed to have a large-scale biconical outflow structure (e.g. Cecil, Bland & Tully 1990; Arribas, Mediavilla & Garcia-Lorenzo 1996; Pogge 1988; Crenshaw & Kraemer 2000). Material within this bicone has been observed in the [O III]λ5007 line to be moving outward from the nucleus at velocities of ∼3000 km s^{-1} at a position angle of ∼32°, believed to be radiatively accelerated by the AGN at the galaxy's centre (Pogge 1988; Cecil et al. 2002; Dopita et al. 2002b). The outflow in [O III] can be seen in Fig. 1(b) with log([O III]/Hβ) values near unity, extending from the centre of the galaxy to the north-east. Material with high values of log([O III]/Hβ) is also seen to the south-west of the galaxy, partially obscured by the disc of the galaxy. This ejecta is aligned with the radio jet seen from this galaxy, which has a measured position angle of 34° (e.g. Wilson & Ulvestad 1983, 1987; Pogge 1988; Gallimore et al. 1996). The models from Das

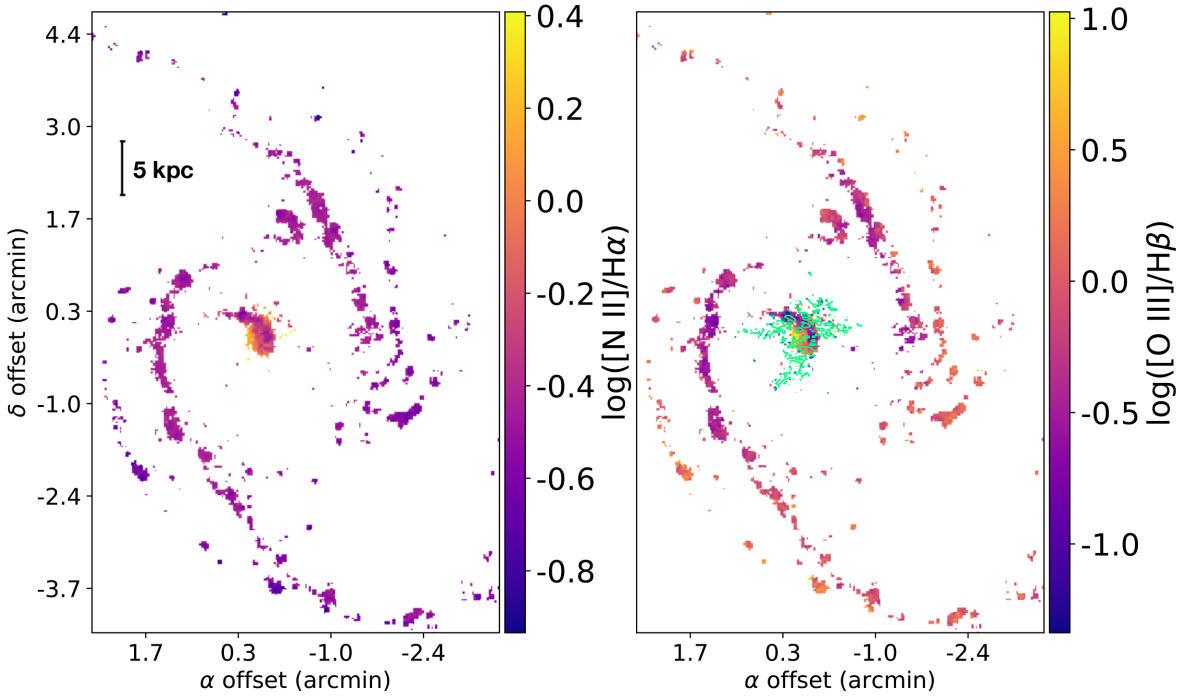

(a) NGC 1365

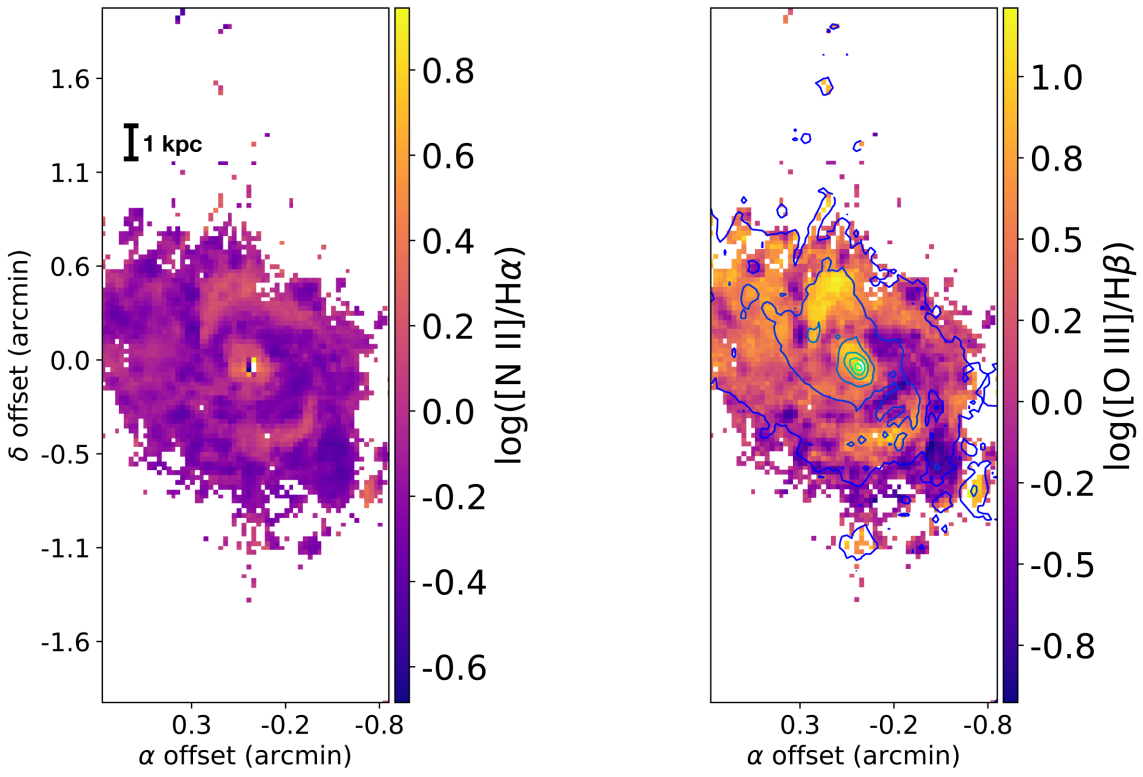

(b) NGC 1068

Figure 1. [N II]/H α and [O III]/H β distribution maps for NGC 1365 and NGC 1068. Contours of [O III] with a signal-to-noise ratio greater than 3 are included on the [O III]/H β maps. The [O III] contours are shown for the inner 7 kpc of NGC 1365, ranging from log([O III]) = 1.5 (light green) to log([O III]) = 0.5 (deep blue) 10^{-17} erg s^{-1} cm^{-2} arcsec^{-2} in increments of 0.5 dex. For NGC 1068, contours for the whole map are shown, ranging from log([O III]) = 5.6 (light green) to log([O III]) = 1.6 (deep blue) 10^{-17} erg s^{-1} cm^{-2} arcsec^{-2} in increments of 0.8 dex.

et al. (2006) (especially their fig. 10) which attempt to model the bicone give an opening angle of ∼80° and position angle of ∼30°. Values of parameters relating to the geometry of the bicone measured by Das et al. (2006) agree closely with those calculated by Crenshaw & Kraemer (2000), with the exception of the value for the bicone position angle for which Crenshaw & Kraemer (2000) suggest 15°. Poncelet, Sol & Perrin (2008) also measure a value for the bicone orientation using emission lines in the infrared which is in closer agreement to that suggested by Crenshaw & Kraemer (2000). Poncelet et al. (2008) suggest a bicone orientation with a position angle of ∼10°. The position angle suggested by Poncelet et al. (2008) is in better agreement with the *HST* [O III] image results from Evans et al. (1991). Poncelet et al. (2008) do however agree with the opening angle of the bicone calculated by Das et al. (2006), finding an opening angle of ∼82°. However, as mentioned by Goosmann & Matt (2011), derivation of the actual geometry of the ionization bicone close to the centre is not straightforward when observations have large spatial scales. Instead, they propose X-ray polarimetry to constrain the geometry of the innermost outflows.

3 OBSERVATIONS AND DATA REDUCTION

3.1 Observations

TYPHOON is a survey which uses the PrISM, also known as the 'step-and-stare' or 'stepped-slit' method to construct 3D data cubes of 100 of the closest and largest galaxies in the Southern hemisphere. The survey is being undertaken on the 2.5 m du Pont telescope at the Las Campanas Observatory in Chile. While not using an IFU *per se*, the observations are made by progressively stepping a long-slit aperture across a galaxy to mimic the effect of an IFU. Thus, the end product is a high spectral resolution data cube. The data cubes produced from the TYPHOON/PrISM survey are highly resolved, with a spatial resolution of ∼4–5 pc at best (Sturch & Madore 2012). Further details about the TYPHOON/PrISM survey will be explained in a forthcoming publication (Seibert et al. in preparation).

NGC 1365 was observed using the Wide Field reimaging CCD (WFCCD) imaging spectrograph on the du Pont telescope. The WFCCD has a field of view of 25 arcmin and we construct the 3D data cube using a custom long-slit (18 arcmin × 1.65 arcsec; 0.5 arcmin^2) which was placed along the north–south direction and progressively scanned across the galaxy through stepping and staring. Each pointing position was integrated for 600 s before the slit was moved by one slit width in the east–west direction for the next integration. This procedure was repeated until the optical disc of NGC 1365 was covered. In total, 223 observations covering an area of approximately 6 arcmin × 18 arcmin were taken during 15 nights over four observing runs in 2011 November, 2016 January, 2016 February, and 2016 August. NGC 1068 was also observed using the WFCCD imaging spectrograph on the du Pont telescope, with 63 observations taken between the 8th and 11th of 2012 October inclusive. The observations cover an area of 1.73 arcmin × 18 arcmin, centred on the nucleus and inner star-forming ring. Each exposure was also integrated for 600 s. Observations were performed only when the seeing was less than the slit-width of 1.65 arcsec. Spectrophotometric flux standards were observed each night.

3.2 Data reduction

The data are reduced using standard long-slit data reduction techniques. The wavelength calibration has a typical root-mean-square value 0.05 Å for the entire data set. Flux calibration is accurate to 2 per cent at the spaxel scale over the range of 4500–7500 Å. The reduced long-slit 2D spectra are tiled together to form the 3D data cube. The final reduced data cube covers a wavelength range of 3650–8150 Å, with spectral and spatial samplings of 1.5 Å and 1.65 arcsec, respectively. From fitting Gaussians to field stars in the reduced data cube, we estimate that the full width half-maximum of the point spread function is approximately 2 arcsec, which corresponds to approximately 169 pc at the assumed distance of roughly 18 Mpc. The instrumental dispersion is approximately 3.5 Å (σ corresponds to $R \approx 850$ at 7000 Å).

The colour-composite images extracted from the reduced data cube are shown in the left-hand panels of Fig. 2 for both galaxies NGC 1365 and NGC 1068. The Hα flux maps derived from the data cube for both galaxies are shown in the right-hand panels of Fig. 2. We use the emission line fitting tool LZIFU (Ho 2016; Ho et al. 2016) to measure emission line fluxes from the raw data, following the method outlined in Ho et al. (2017). The flux of Hα emission peaks at the centre of the galaxy for both galaxies. Hence, we use the spaxel containing the highest value of Hα flux as the centre of the galaxy, from which we measure our radial offsets.

The large-scale distribution of Hα is seen to follow the spiral arms in both galaxies. However, the centres of both NGC 1365 and NGC 1068 have been shown to be dominated by harder ionizing processes, such as AGN and shocks (see Section 2), resulting in outflows seen in emission lines such as [O III]λ5007. Their centres also contain significant star formation, such as the nuclear 1 kpc diameter starburst ring in NGC 1068 (e.g. Wilson et al. 1991). Therefore, while some clear AGN-driven structures can be detected using single lines like the biconical outflow in the [O III] map of NGC 1365 in Fig. 3, most lines towards the centre arise from some combination of star formation and AGN affected gas. This is most clearly seen in Fig. 1, which shows increases towards the nucleus in both the [N II]/Hα and [O III]/Hβ ratios. We note that the line ratio maps in Fig. 1 do not show evidence of a biconical outflow in NGC 1365 due to low signal-to-noise in the Hβ line. Hence, we make use of the BPT diagram and each galaxy's mixing sequence to separate star formation and AGN activity. For this work, we apply a consistent signal-to-noise cut of 3 on all emission lines in the BPT diagram (Hα, Hβ, [O III], [N II]).

3.2.1 *Correcting for saturation in NGC 1068*

The emission lines affected by saturated pixels include [O III]λλ4959,5007, Hα, and [N II]λλ6543,6584. In the pipeline, pixels that are saturated are flagged and carried through as 'NaN' pixels. We reproduce the line profile by performing a fit to the unsaturated emission line(s). For spaxels with saturated lines, we use IDL/MPFIT to fit the Hβ profile with a two-component Gaussian.

The [O III]λλ4959,5007 profile with saturated (NaN) pixels is fitted with IDL/MPFIT using a two-component Gaussian with the redshift and velocity width of the Gaussian components fixed to the values derived from the Hβ fit. The line peaks, continuum level, and continuum slope are allowed to vary (the [O III]λλ4959,5007 ratio is held fixed at 1:3), using the Gaussian shape and the unsaturated wings of the line to constrain the missing data. Any 'NaN' pixels in the region of [O III] are replaced with the value from the resulting fit.

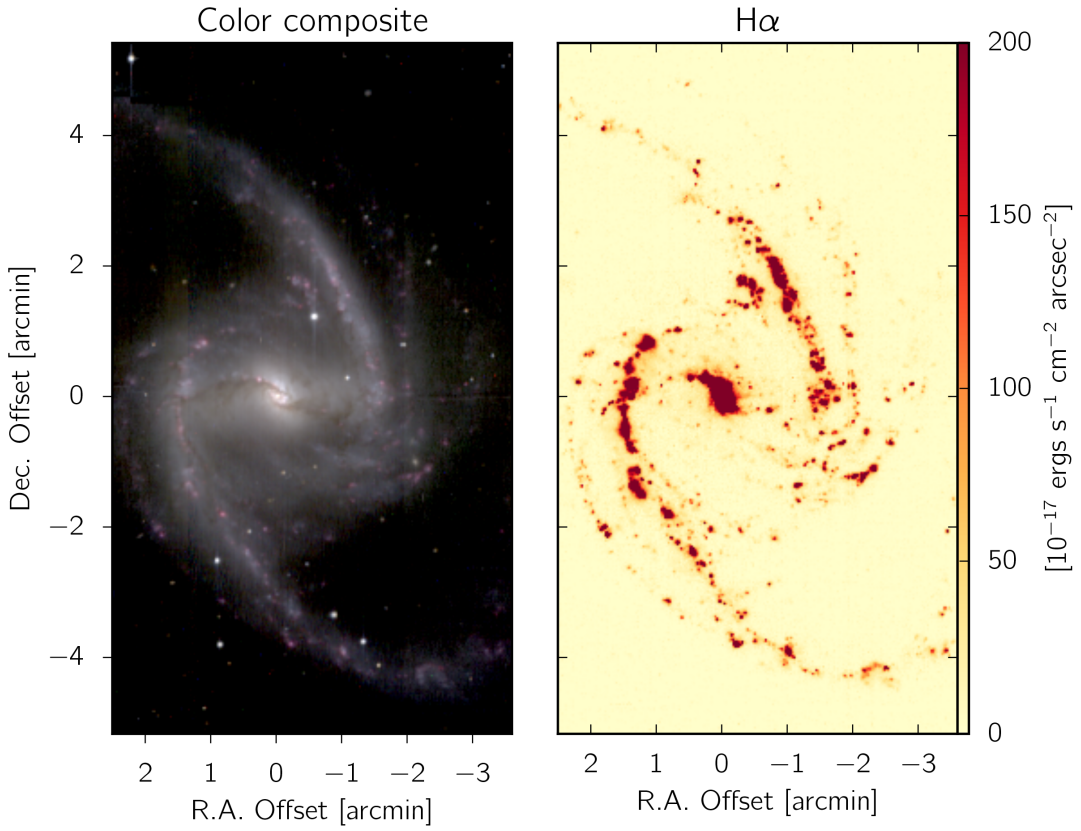

(a) NGC 1365

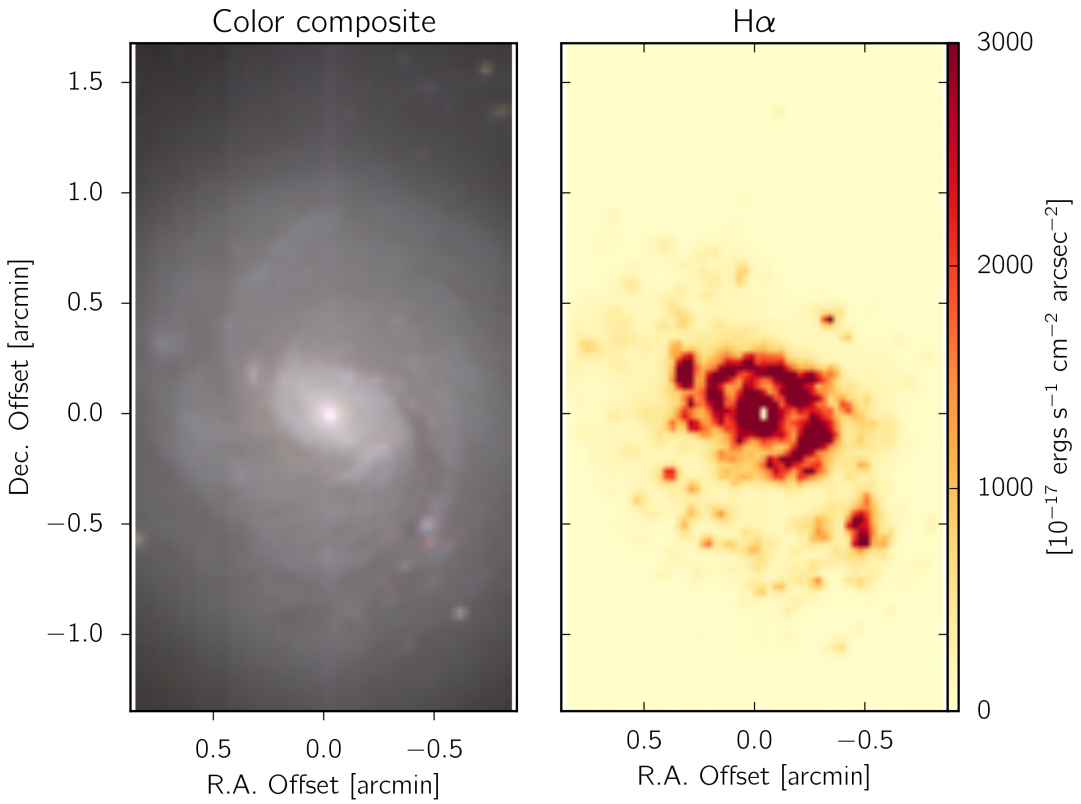

(b) NGC 1068

Figure 2. Colour composite (*BVR*) and H α maps for NGC 1365 and NGC 1068 from the TYPHOON data cubes. For both images (and all hereafter), north is vertically upwards, and east to the left.

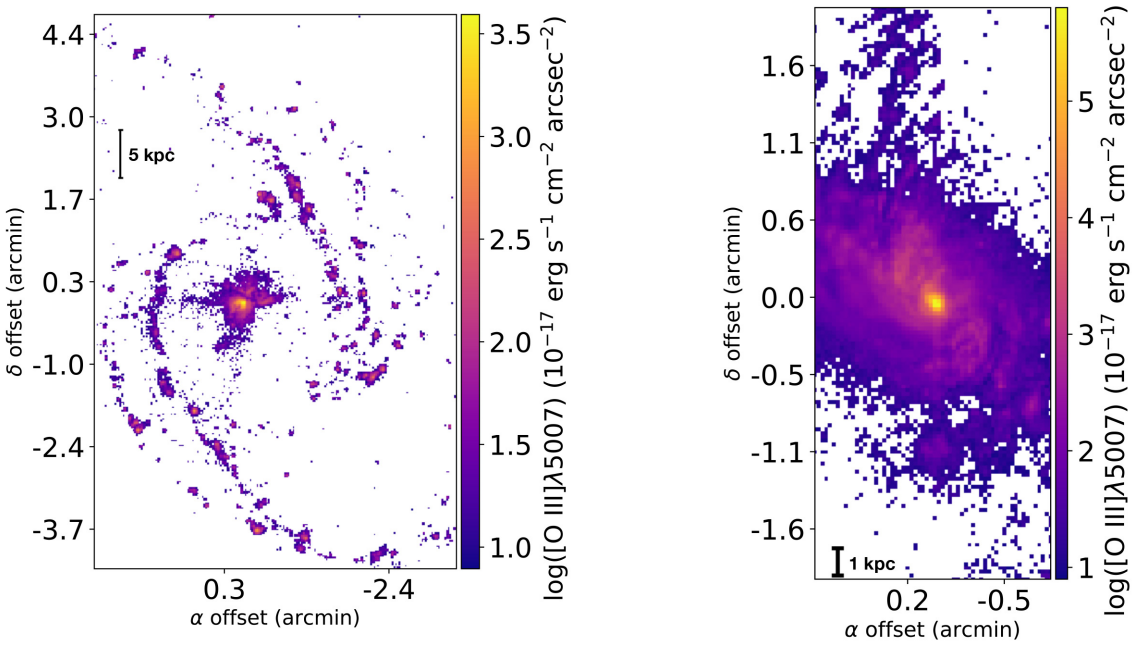

(a) NGC 1365

(b) NGC 1068

Figure 3. -[O III] distribution maps for NGC 1365 and NGC 1068.

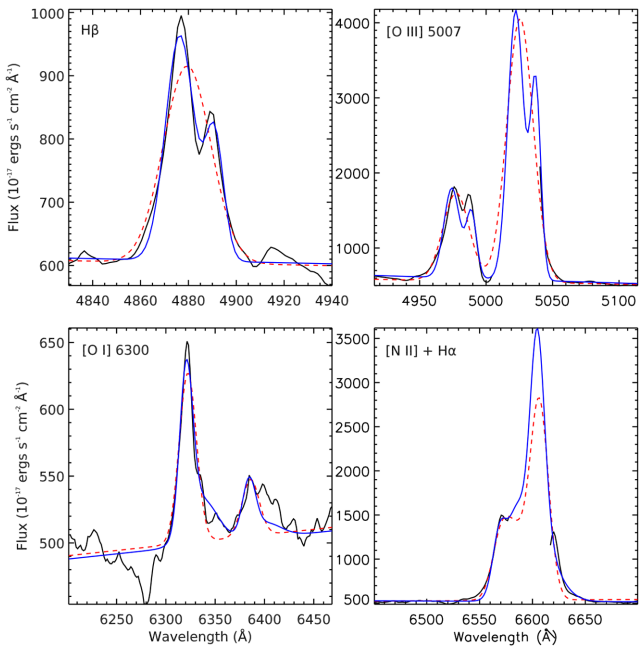

Figure 4. The fitting correction applied to the NGC 1068 data cube for NaN spaxels at the centre. Figure shows corrections to the H β, [O III], [O I], [N II], and H α emission lines. The one-component Gaussian fits are shown in red, while the two-component fits are shown in blue.

This process is repeated using the [O I]$\lambda\lambda$6300,6363 doublet to generate a two-component Gaussian used to fit the [N II]$\lambda\lambda$6543,6584 + H α region in the same fashion (redshift and width are fixed, the [N II]$\lambda\lambda$6543,6584 ratio is fixed to 1:3, the peaks of the [N II] and H α lines are allowed to vary). The example in Fig. 4 shows the H β (top left) and [O I] (bottom left) fits – a single component fit is shown in red and the two-component fit is shown in orange. The fits

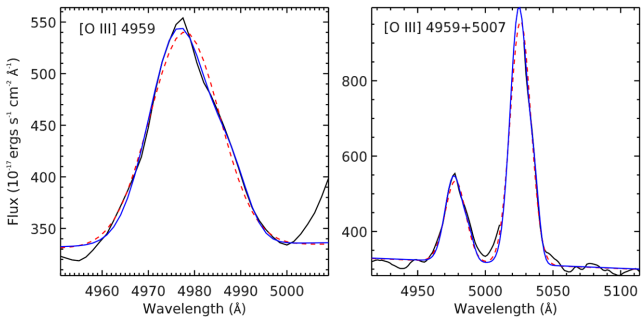

Figure 5. Figure showing the fit to the [O III]λ4959, used to fit the [O III]$\lambda\lambda$4959,5007 when the signal-to-noise in the H β profile is too low to provide reliable fit parameters. The one-component Gaussian fits are shown in red, while the two-component fits are shown in blue.

to [O III] (upper right) and [N II]+H α (bottom right) using the same Gaussian components are shown on the right.

Finally, there are some spaxels where the signal-to-noise in the H β profile is too low to provide a reliable fit to be used for the [O III] doublet. For these four spaxels, we fit the [O III]λ4959 line to generate the two-component Gaussian widths and redshifts, and apply the results to the [O III]$\lambda\lambda$4959,5007 simultaneously with the resulting widths and redshifts fixed. In Fig. 5, the left-hand panel shows the fit to [O III]λ4959 and the right-hand panel shows the combined [O III]$\lambda\lambda$4959,5007 fit using the parameters from the [O III]λ4959 fit. Again a single-component Gaussian is shown in red and a two-component Gaussian is shown in orange.

The spaxels with these corrections applied are located at the following (α, δ) arcminute offsets from the centre of the galaxy): (−0.028, −0.054), (−0.055, −0.054), (−0.028, −0.027), (−0.055, −0.027), (−0.028,0.000), (−0.055,0.000), (0.000,0.027), (−0.028,0.027), (−0.055,0.027), (0.000,0.054), (−0.028,0.054), (−0.055,0.054), (−0.028,0.081), (−0.055,0.081).

In total, when considering spaxels with a signal-to-noise cut greater than 3 in all the emission lines on the BPT diagram, the percentage of spaxels with a correction applied is only 0.5 per cent.

4 PHOTOIONIZATION MODEL GRIDS

The photoionization grids used during this work were created using the photoionization code `MAPPINGS V.1`. We compute separate model grids for both the star formation region and the AGN region of the BPT diagram, described subsequently.

4.1 Starburst model grid

The parameters involved in the creation of the starburst model grid are based on the findings and recommendations given by D'Agostino et al. (). We consider all aspects of the HII region, including a stellar cluster and physical structure of the region.

4.1.1 Ionizing stellar spectrum

To synthesize the ionizing stellar spectrum, we use the stellar population synthesis code Stochastically Lighting Up Galaxies (SLUG; da Silva, Fumagalli & Krumholz 2012; Krumholz et al. 2015). The stellar spectrum is created using the initial mass function of Kroupa (2002), the Geneva 'High' mass-loss (HIGH) stellar evolutionary tracks published in Meynet et al. (1994), and the stellar atmospheres of Lejeune, Cuisinier & Buser (1997) with the addition of updated Wolf–Rayet (WR) and OB star atmospheres from Hillier & Miller (1998) and Pauldrach, Hoffmann & Lennon (2001), respectively. We favour the use of certain stellar models based on updates to the input physics from previous models. The Geneva group's HIGH stellar tracks include a correction to the definition of stellar effective temperature at the WR phase. Similarly, specialized modelling of WR stars by Hillier & Miller (1998) and OB stars by Pauldrach et al. (2001) include updated physics to model both processes of line blanketing and line blocking, as well as a revised EUV and X-ray radiation model as a result of shock cooling zones in the OB stellar winds. We assume a stellar population at 10 Myr, undergoing constant star formation at a rate of $1\,M_{\odot}\,yr^{-1}$. We use an age of 10 Myr, as 10 Myr is the age at which 99.9 per cent of ionizing photons have been released for a single stellar generation undergoing constant star formation (e.g. Charlot & Longhetti 2001; Feltre, Charlot & Gutkin 2016). Hence, the shape of the stellar spectrum varies negligibly beyond this point. Despite the fact that we resolve individual H II regions harbouring a single stellar cluster in galaxies using TYPHOON data, we use models which assume a continuous star formation history. As we resolve individual H II regions across the entire galaxy (see Fig. 6), it is fair to assume the initial conditions and rates of star formation within each H II region differ throughout the galaxy, especially considering galaxies containing an AGN with a rich history of large-scale outflows. Hence, our models consider radiation from stellar clusters of all ages up to and including 10 Myr.

4.1.2 H II region structure

We assume a spherical geometry for our H II region, and adopt the elemental abundance solar reference of Anders & Grevesse (1989), and metallicity scaling prescription of Nicholls et al. (2016), matching the stellar abundance to the overall metallicity of the stellar tracks. Our model includes dust, using the elemental depletion pattern of Jenkins (2014), with a fraction of 0.3 of the carbon dust in the form of polycyclic aromatic hydrocarbons. We use five metallicities in our starburst grid, with metallicities of $Z = 0.001$, 0.004, 0.008, 0.020, and 0.040. Z here refers to the mass fraction of heavy elements (elements heavier than helium), defined by the relationship $X(\mathrm{H}) + Y(\mathrm{He}) + Z = 1$. The range of metallicities sufficiently covers the metallicity range measured in both galaxies NGC 1365 and NGC 1068. We use the R_{23} metallicity diagnostic from Kobulnicky & Kewley (2004) to measure the range of metallicity in both galaxies. This is discussed further in Section 5.1. We include a range of the ionization parameter $Q(N)$, defined as the number of ionizing photons emitted from the source relative to the number density of all ions in the nebula, with values of $\log(Q(N)\,\mathrm{cm}^{-2}\mathrm{s}^{-1})$ from 6.5 to 8.5 inclusive, in increments of 0.25 dex. The range of ionization parameter is comparable to that used by Kewley et al. (2001). We compute our model in isobaric conditions, setting the initial pressure of the H II region to be $P/k = 8 \times 10^5\,\mathrm{K\,cm}^{-3}$. Under the assumption of an H II region initial temperature of 8000 K, this approximately corresponds to an electron density of $n = 100\,\mathrm{cm}^{-3}$. Fig. 7 shows the electron density distribution across both NGC 1365 and NGC 1068 calculated using the [S II] ratio, showing an electron density of $n = 100\,\mathrm{cm}^{-3}$ to be a reasonable assumption in the star-forming regions of both galaxies. Our model is assumed to be radiation-bounded, and hence the model is terminated once 99 per cent of H II recombination has occurred.

4.2 AGN model grid

Our AGN models are computed assuming a plane-parallel geometry, and use the same definitions for the abundance pattern and metallicity scaling, and ionization parameter as our starburst model described in Section 4.1.2. We use six metallicities when computing our AGN model grids, with values of $Z = 0.001$, 0.004, 0.008, 0.020, 0.040, and 0.060. However, the low metallicities used in these grids are arguably redundant, as low-metallicity AGNs are rare (e.g. Groves, Heckman & Kauffmann 2006). In increments of 0.25 dex, the ionization parameter varies from $\log(Q(N)\,\mathrm{cm}^{-3}) = 7.0$ to 11.0 inclusive.

We compute the AGN models also in isobaric conditions, however the value of initial pressure differs between the models used for NGC 1365 and NGC 1068. For NGC 1365, we use an initial pressure of $P/k = 2 \times 10^7$, and for NGC 1068, $P/k = 2 \times 10^8$. Under the assumption of a narrow-line region initial temperature of 20 000 K, this corresponds to electron densities of $n = 1000$ and $10\,000\,\mathrm{cm}^{-3}$ for NGC 1365 and NGC 1068, respectively, supported through the density calculation from the [S II] ratio in Fig. 7.

The AGN region models are computed with a power-law spectrum of the form $c\nu^{\alpha}$ (Groves et al. 2004), fixing $\alpha = -1.2$. Lower values of α have been historically favoured (~ -1.4 to ~ -2.0; e.g. Groves et al. 2004; Belsole, Worrall & Hardcastle 2006), however we find lower values of α fail to completely explain the TYPHOON data on the BPT diagram. Further justification on the use of $\alpha = -1.2$ is discussed in Appendix A. The value of α however has been known to vary wildly amongst AGNs (e.g. see detailed catalogue of AGNs by Ackermann et al. 2011).

5 THE STARBURST–AGN MIXING SEQUENCE

As demonstrated by Kewley et al. (2001) and Kauffmann et al. (2003), star-forming galaxies lie along a tight curve on the BPT diagram. However, as an AGN increases in activity until it completely dominates over emission from star formation, the galaxy moves off this star-forming sequence on to a 'mixing sequence' (e.g. Kewley

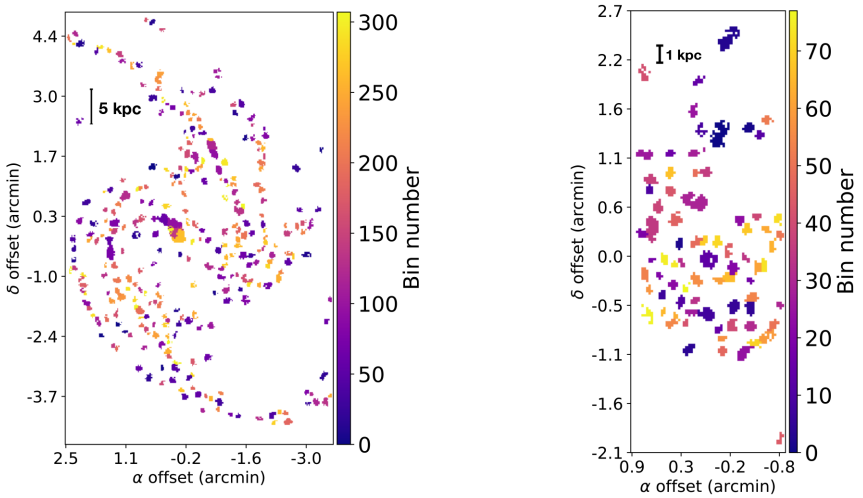

(a) NGC 1365 (b) NGC 1068

Figure 6. Figure showing location of H II regions in NGC 1365 in (a) and NGC 1068 in (b). These H II regions were identified using HIIPHOT, developed by Thilker, Braun & Walterbos (2000).

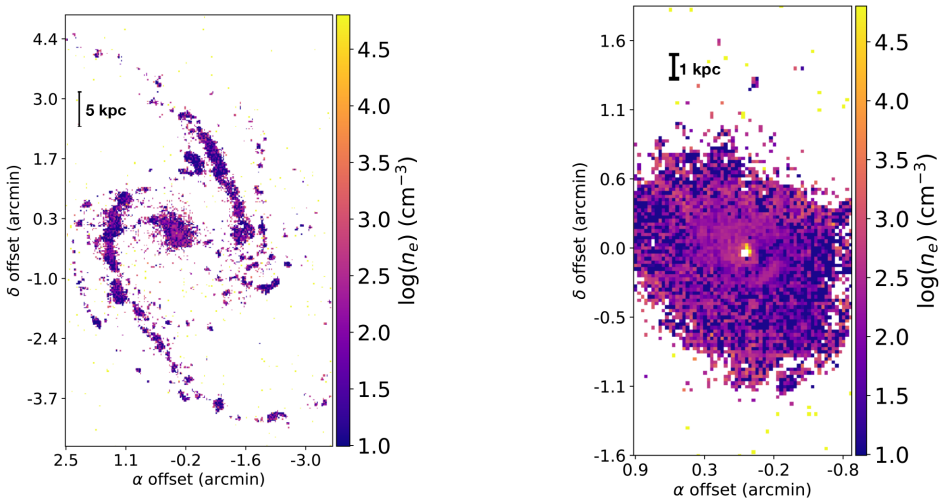

(a) NGC 1365 (b) NGC 1068

Figure 7. Figure showing range of electron density across both NGC 1365 in (a) and NGC 1068 in (b).

et al. 2006). As discussed by Kewley et al. (2001) and demonstrated empirically by Davies et al. (2014a,b), the relative fractional contribution of star formation and the AGN to the emission line luminosity can be determined from this mixing sequence.

Davies et al. (2014a,b) used 'basis points' to define empirical 100 per cent starburst and 100 per cent AGN positions on the BPT diagram. The starburst and AGN basis points were assigned to the spaxels which contained the lowest and highest [O III]/H β ratios, respectively. These basis points corresponded to 0 and 100 per cent AGN activity, respectively. All other spaxels were assigned an AGN fraction between 0 and 100 per cent corresponding to their star-forming distance (d_{SF}; Kewley et al. 2006) along the line between the two basis points. The star-forming distance d_{SF} is a measure of a spaxel's (or galaxy's) offset in its [N II]/H α and [O III]/H β ratios from the star-forming sequence on the BPT diagram, mapped out by pure star-forming galaxies in SDSS (see Kauffmann et al. 2003). The starburst basis point was defined as having a $d_{SF} = 0$. The complement to the AGN fraction with respect to 100 per cent is considered to be the relative fraction of emission from star formation. Using data from the TYPHOON survey, we extend this method, described below.

The result of applying the method described by Davies et al. (2014a,b) to NGC 1365 from the TYPHOON survey is shown in Fig. 8. The method from Davies et al. (2014a,b) when applied to IFU data shows AGN fractions of up to ∼50 per cent for several spaxels along the star-forming sequence of NGC 1365. These spaxels are found below the Kauffmann line, which is considered to be the upper limit of pure star formation.

5.1 Use of photoionization grids

We use the photoionization grids described in Section 4 to aid in the selection of the basis points. The basis points selected by Davies et al. (2014a,b) for their starburst–AGN mixing work are purely

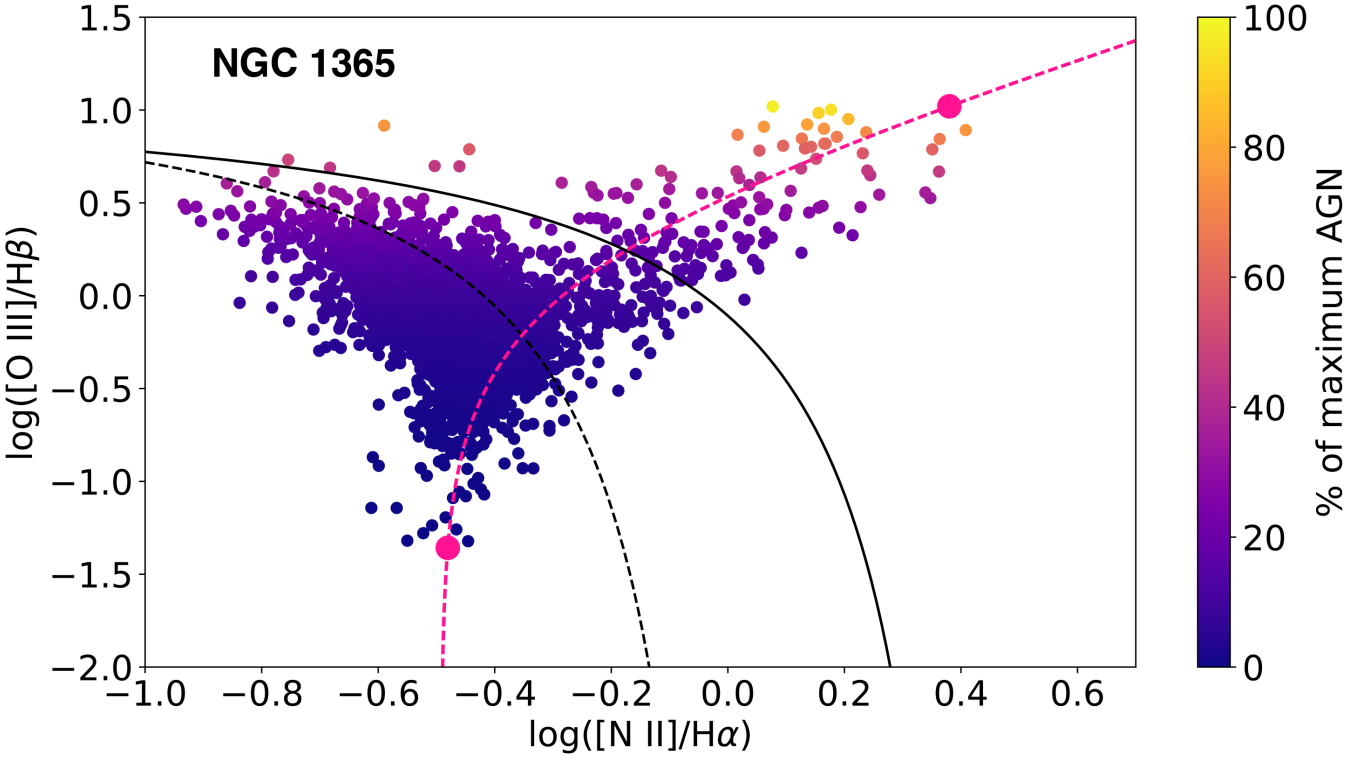

Figure 8. The AGN fraction for NGC 1365, using the old calculation by Davies et al. (2014a,b). The method from Davies et al. (2014a,b) gives AGN fractions of up to ∼50 per cent for some spaxels below the Kauffmann line – a well-known empirical line which signifies the upper limits of pure star formation.

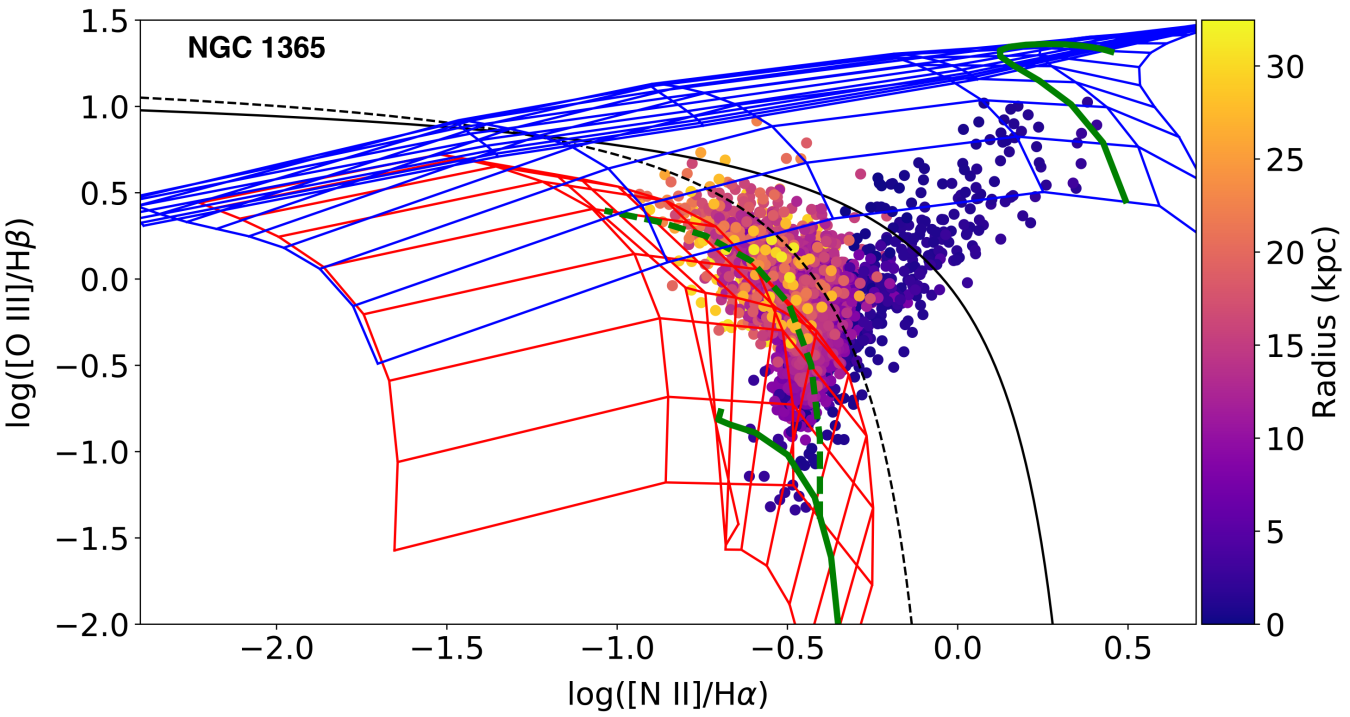

Figure 9. The BPT diagram of NGC 1365, with each spaxel coloured according to radius from the centre of the galaxy. The black dashed curve is the Kauffmann et al. (2003) empirical maximum starburst line, and the black solid line is the Kewley et al. (2001) theoretical maximum starburst line. The H II region grid is shown in red, and the AGN grid is shown in blue. The solid green grid lines on both grids represent the metallicity at the centre of the galaxy, and the dashed green grid line on the H II region grid represents the metallicity at the edge of the galaxy. Both metallicity values are stated in Table 1.

Table 1. Derived quantities for NGC 1365 and NGC 1068 for use on the BPT diagram.

Galaxy	Metallicity ($Z_\odot$)		Basis Point Coordinates [log([N II]/H α), log([O III]/H β)]				
	Edge	Centre	SB_1	SB_2	SB_3	AGN_1	AGN_2
NGC 1365	0.55	1.42	(−1.01, 0.39)	(−0.64, −0.86)	(−0.42, −1.27)	(0.24, 1.14)	(0.46, 0.62)
NGC 1068	1.02	1.41	(−0.52, −0.19)	(−0.48, −0.99)	(−0.38, −1.49)	(0.22, 1.31)	(0.49, 0.71)

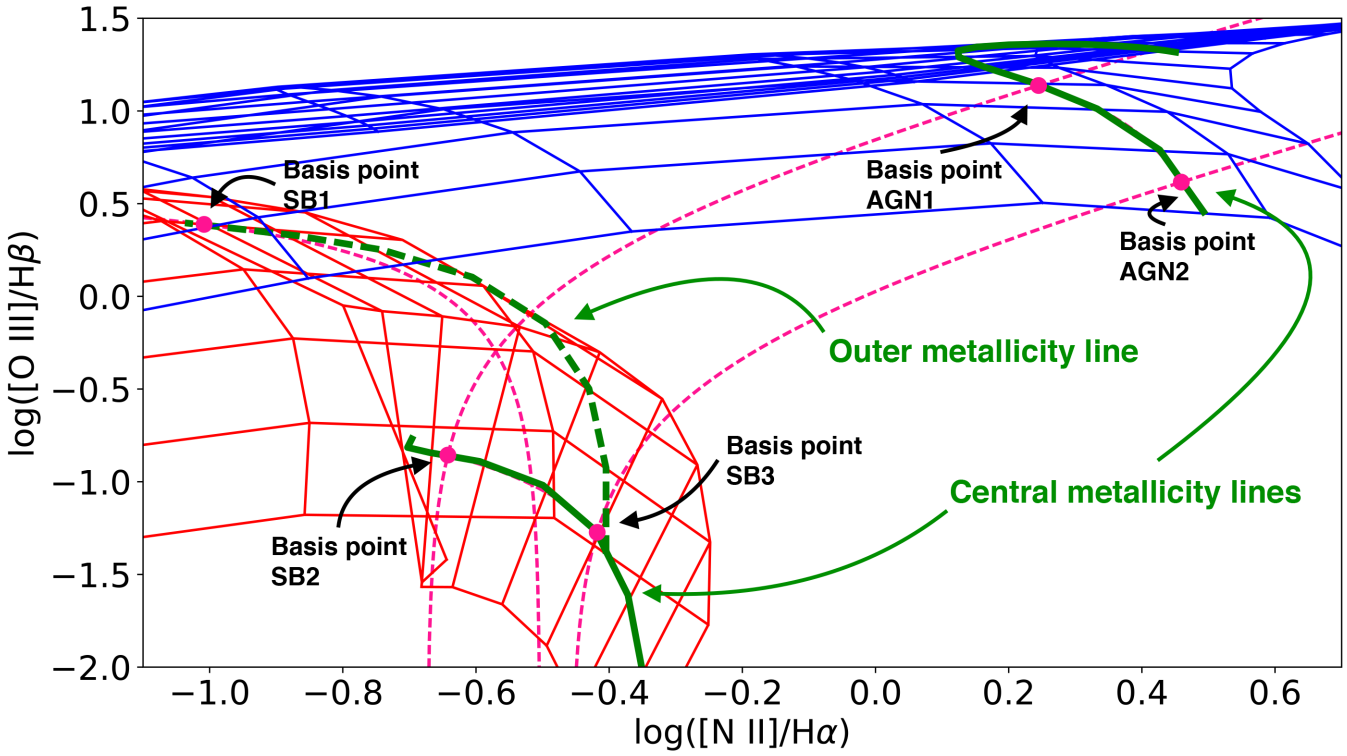

Figure 10. The basis points exhibited on the photoionization grids, with the location of each constrained using the metallicity measurements of NGC 1365. The starburst basis points SB1, SB2, and SB3 define the starburst basis line, while the basis points SB2, SB3, AGN1, and AGN2 together define the nuclear column.

empirical. Hence, the basis points contain no physical information about the galaxy. Through the use of photoionization grids, star formation and AGN activity can be separated with the basis points containing physical information about the galaxy, such as the metallicities, ionization parameters, pressures of both the H II and AGN regions, and hardness of the AGN power-law radiation field (Thomas et al. in preparation). In addition, theoretical models also allow the prediction of spectra at other wavelengths.

To constrain the basis points of both the AGN and star-forming grids, we use the independently determined gas-phase metallicity. The R_{23} metallicity diagnostic from Kobulnicky & Kewley (2004) (KK04) was used to diagnose metallicities from H II regions within the galaxy. These H II regions were identified using the IDL routine HIIPHOT, developed by Thilker et al. (2000). The H II regions were found to be located throughout the galaxy, thus making possible the calculation of metallicity gradients from the central regions to the outskirts of both galaxies. The location of the H II regions across NGC 1365 and NGC 1068 can be seen in Fig. 6. The metallicities for the central and outer regions of both NGC 1365 and NGC 1068 can be found in Table 1.

Seen in Fig. 9, coloured by radius from the centre of the galaxy, is the presence of a large star-forming sequence in NGC 1365. This star-forming sequence extends from the nucleus to the outermost regions of the galaxy. The starburst grid shows a metallicity gradient within this star-forming sequence, beginning at a high metallicity within the nucleus, and extending to a low metallicity at the edges of the galaxy.

We used the metallicity calculations to construct extra lines on the photoionization grids, corresponding to the metallicities of the central and outer regions of the two galaxies. All basis points are positioned along these new grid lines, depending on the region of the galaxy for which they correspond. The positions of basis points SB1, SB2, and SB3 are defined by the starburst grid, while the positions of basis points AGN1 and AGN2 are defined by the AGN grid. Basis point SB1 is positioned along the line corresponding to the outer metallicity of the galaxy, at the edge of the star-forming sequence of spaxels. Basis points SB2 and SB3 are positioned along the line of central metallicity at the nuclear region of the star-forming sequence. Basis points AGN1 and AGN2 are also positioned along the line of central metallicity. The basis points are placed along the lines of constant metallicity such that they encompass the spread in ionization parameter in the data (see Section 5.3). The starburst basis points SB1, SB2, and SB3 define the *starburst basis line*, described in Section 5.2. Basis points SB2, SB3, AGN1, and AGN2 altogether define the *nuclear column*, defined in Section 5.3. As an example, we show all five basis points located on the photoionization grids

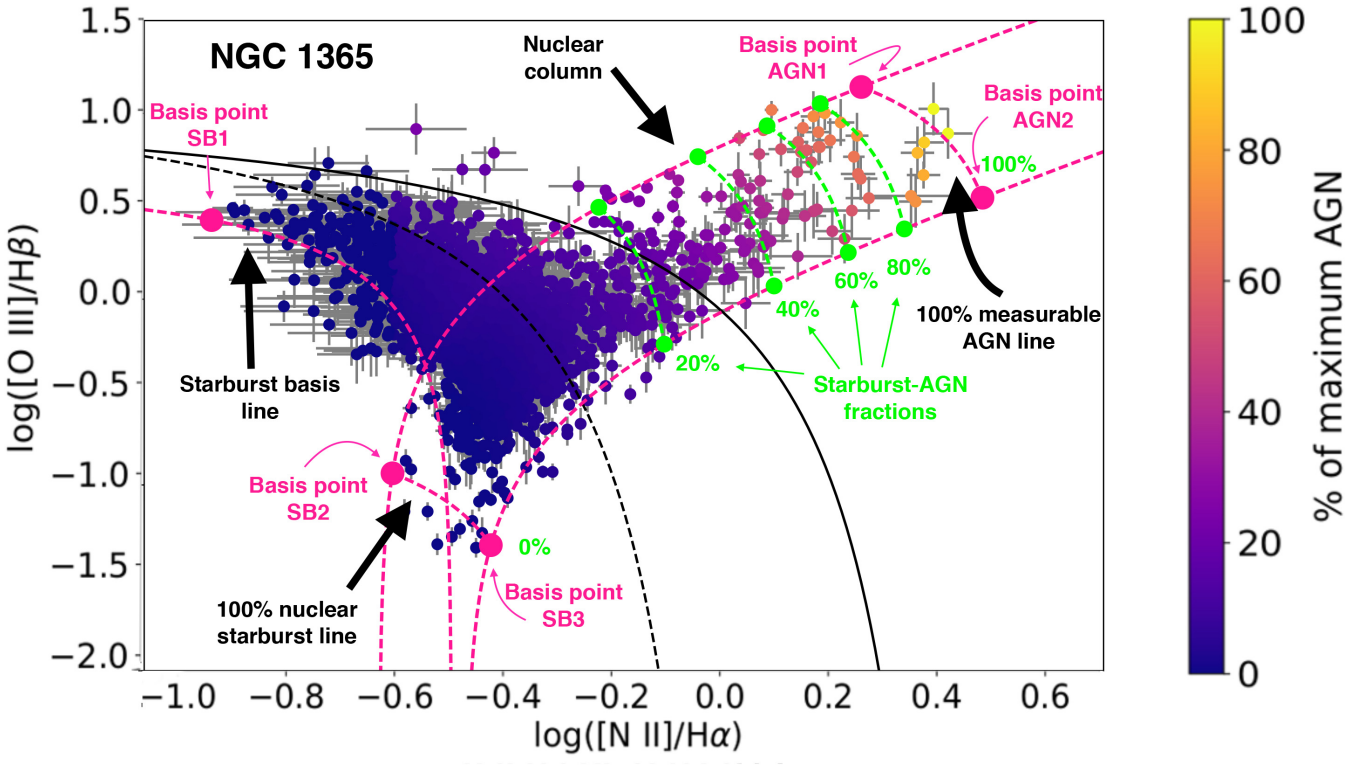

Figure 11. The BPT diagram for NGC 1365 showing the fractional contribution of AGN excited gas to the Hα line using our new calculation method. This figure also overlays the original Kauffmann et al. (2003) and Kewley et al. (2001) AGN diagnostic lines (black lines, Fig. 9), the new basis points and mixing curves based on our model grids (pink points and lines, Fig. 10 and Section 5), and the resulting starburst–AGN mixing sequence (green curves).

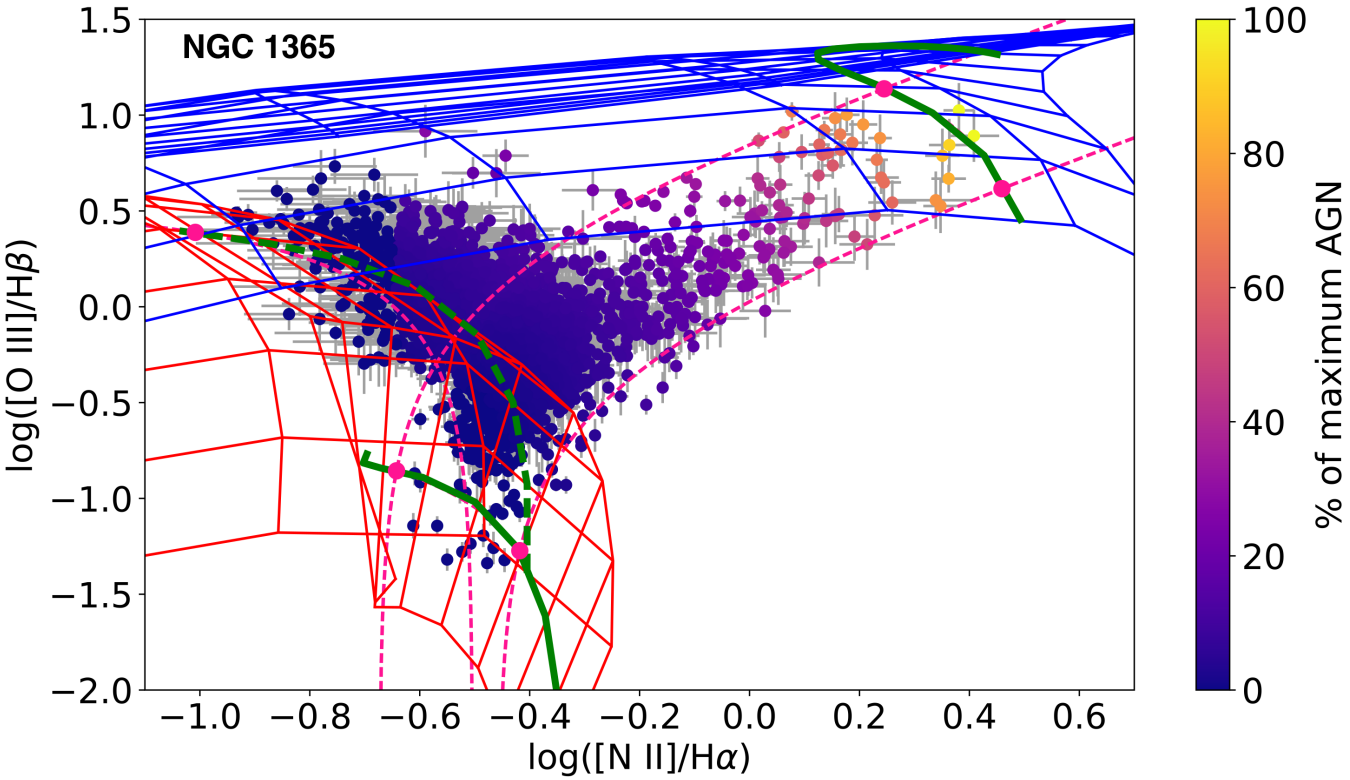

Figure 12. AGN fraction [O III]/Hβ versus [N II]/Hα diagram for NGC 1365.

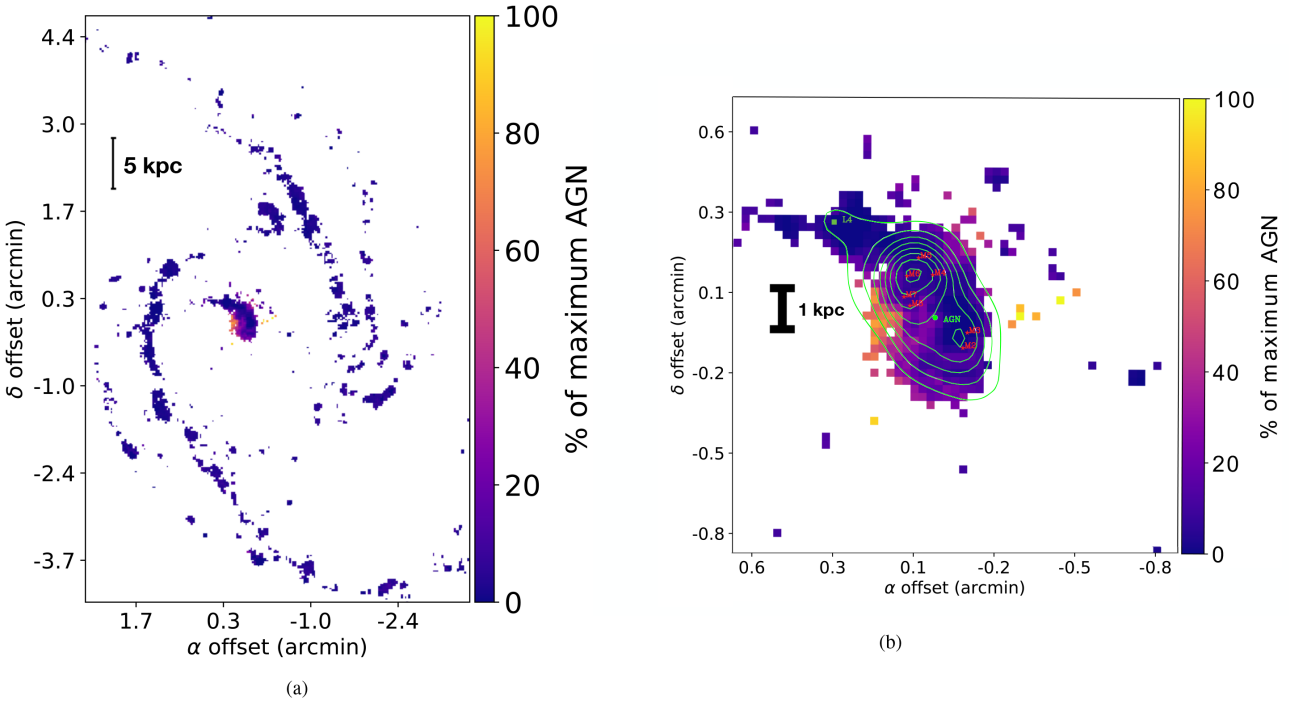

Figure 13. Map of NGC 1365 (a), with spaxels coloured to the [O III]/H β versus [N II]/H α AGN fraction. The nucleus of NGC 1365 is shown in (b), overlaid with an image from Alonso-Herrero et al. (2012) showing star-forming clusters identified by Galliano et al. (2005) (red stars, M2,..., M8), the H α hotspot L4 from Alloin et al. (1981) and Kristen et al. (1997), and light green contours showing the 70 μm flux distribution from Herschel PACS (square-root flux scaling, flux density of 85.5 Jy in the inner 15 arcsec; Alonso-Herrero et al. 2012). The contours are in a square-root intensity scale, with flux of 70 μm mid-IR emission.

in Fig. 10, using the central and outer metallicities of NGC 1365 to determine their locations. Fig. 10 also demonstrates the basis points defining the starburst basis line, and the nuclear column.

5.2 Starburst basis line

Davies et al. (2014a,b) assign a star-forming distance of $d_{\rm SF} = 0$ to the high-metallicity end of the star-forming sequence, as the majority of AGN-dominated galaxies are shown to mix with high-metallicity H II regions (Groves et al. 2006). The high spatial resolution of the TYPHOON IFU data shows a star-forming sequence present in each individual galaxy, following the path mapped out by the pure star-forming galaxies in SDSS (see Kauffmann et al. 2003). By defining a single point as $d_{\rm SF} = 0$, the spaxels on the star-forming sequence which extend out to lower metallicities are given progressively higher values for their star-forming distance. Seen in Fig. 8, lower metallicity star-forming spaxels are designated larger AGN fractions than expected.

We extend the notion of a starburst basis point defined as $d_{\rm SF} = 0$, to a *starburst basis line*. Any spaxel present along the line is defined as having $d_{\rm SF} = 0$. This line is indicated on Fig. 11, extending between the starburst basis point SB1, and the mid-point of the starburst basis points SB2 and SB3.

5.3 Nuclear column

Interestingly, all spaxels seen in the mixing sequence of NGC 1365 in Fig. 9 are located in the nucleus, showing both star formation and AGN activity occurring as nuclear processes. Seen along this mixing sequence in Fig. 9 is a clear spread in the ionization parameter. We further extend the method displayed by Davies et al. (2014a,b) by increasing the number of basis points located at either end of the mixing sequence from one to two, in order to account for this spread in ionization parameter ($\Delta \log Q(N) \sim 0.5$ dex). The result is defined as the *nuclear column*, and indicated in Fig. 11 as extending between the 100 per cent nuclear starburst line, and the 100 per cent measurable AGN line. The nuclear column ensures the star-forming distance in the spaxels along the mixing sequence remains consistent, despite the changes in ionization parameter. The AGN fraction for each spaxel is then determined by each spaxel's distance along a unique line projected between the 100 per cent nuclear starburst line and the 100 per cent AGN line.

5.4 Relative AGN fractions

We calculate the relative AGN fractions for several emission lines for both NGC 1365 and NGC 1068, given as a percentage of the total emission. This calculation is identical to that displayed and described in Davies et al. (2014a). The complement of the AGN fraction with respect to 100 per cent signifies the relative fraction of the total emission from star formation. The total luminosity of any emission line in a given galaxy can be calculated by the following:

$$L_{\rm Tot} = \sum_{i=1}^{n} L_i \, ,$$

where L_i is the luminosity in spaxel i for the emission line in question. The total luminosity of the emission line attributable to AGN activity can be calculated from

$$L_{\rm AGN} = \sum_{i=1}^{n} f_i^{\rm AGN} L_i \, ,$$

where $f_i^{\rm AGN}$ is the AGN fraction in spaxel i. It follows that the relative fraction of emission attributable to AGN activity for the

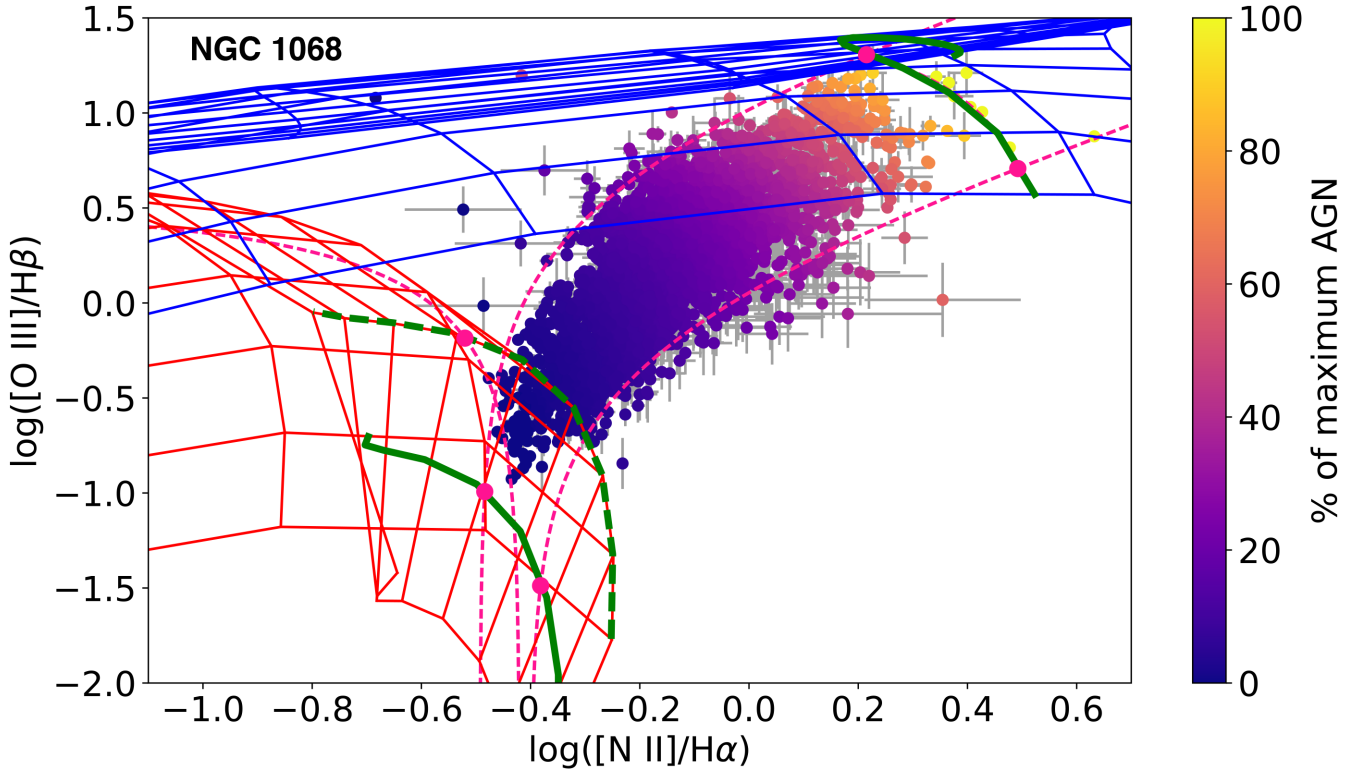

Figure 14. AGN fraction [O III]/H β versus [N II]/H α diagram for NGC 1068.

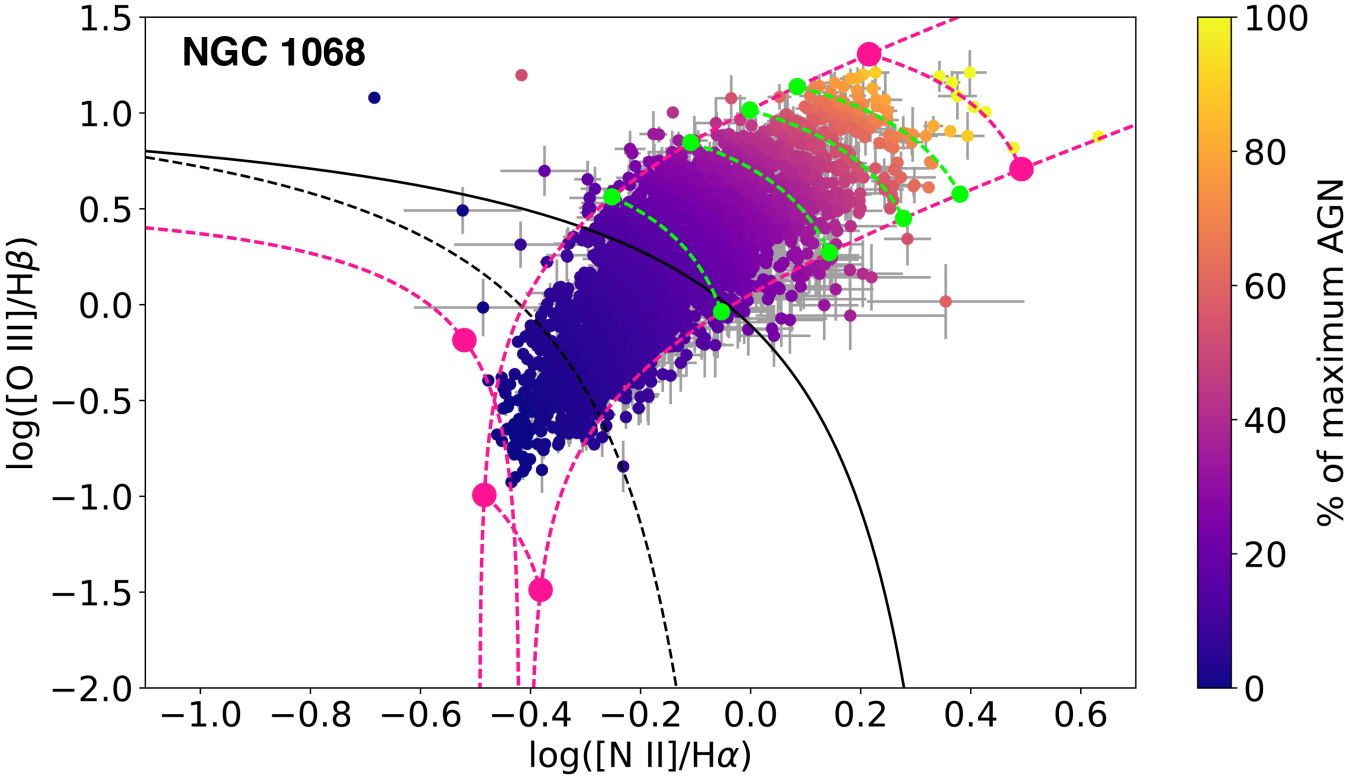

Figure 15. AGN fraction [O III]/H β versus [N II]/H α diagram, without grids for clarity. Green dashed lines indicate 20, 40, 60, and 80 per cent AGN.

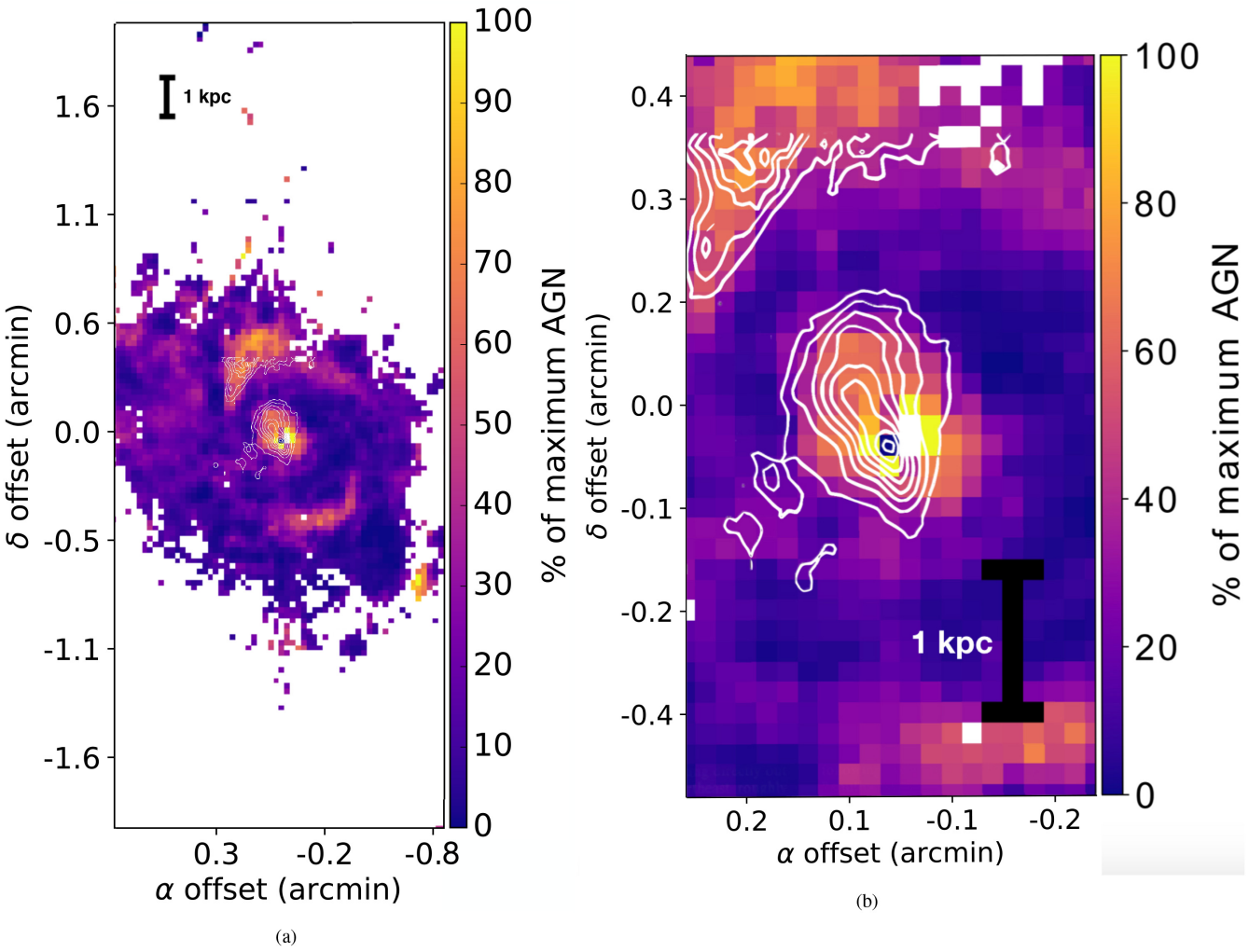

Figure 16. Map of NGC 1068 (a), with spaxels coloured to the O III]/H β versus [N II]/H α AGN fraction. The nucleus of NGC 1068 is shown in (b). The [O III]/(H α + [N II]) contours from Pogge (1988) are shown on NGC 1068 in (a) and (b) in white.

Table 2. (i) The percentage of spaxels showing emission from low surface brightness features. Spaxels showing emission from low surface brightness features are defined as being below the nuclear column. (ii) The radius of equal starburst and AGN domination (AGN fraction = 50 per cent) for varying resolutions for both NGC 1365 and NGC 1068. Values are calculated as averages of distances for spaxels with AGN fractions between 45 and 55 per cent. The errors on these values represent the standard deviation of these sets of distances.

Resolution	Native	330 pc pix^{-1}	500 pc pix^{-1}	1 kpc pix^{-1}
	Percentage of spaxels from low surface brightness features			
NGC 1365	0.03 per cent	0.61 per cent	0.77 per cent	0.20 per cent
NGC 1068	1.29 per cent	2.04 per cent	0.66 per cent	2.11 per cent
	Radii of equal starburst–AGN domination			
NGC 1365	1.35 ± 0.36 kpc	2.49 ± 1.12 kpc	2.79 ± 0.92 kpc	4.26 ± 2.08 kpc
NGC 1068	2.26 ± 1.27 kpc	3.55 ± 1.89 kpc	5.00 ± 1.81 kpc	6.97 ± 2.98 kpc

given emission line is given by

$$f_{\rm Tot}^{\rm AGN} = \frac{L_{\rm AGN}}{L_{\rm Tot}}.$$

Shown in Table 3 are the results of the above calculations for several emission lines. We discuss the results for NGC 1365 and NGC 1068 below individually.

5.4.1 NGC 1365

AGN activity from NGC 1365 has been inferred previously, with studies showing the nucleus of NGC 1365 to be luminous in hard X-rays (e.g. Risaliti et al. 2007, 2013), radio wavelengths (e.g. Sandqvist, Jorsater & Lindblad 1982; Sandqvist et al. 1995), and FUV radiation (e.g. Phillips et al. 1983). Further, the nucleus of NGC 1365 has been shown to produce large fluxes of collisionally

Table 3. AGN fractions for several strong emission lines at varying resolutions for both NGC 1365 and NGC 1068 within the TYPHOON field of view. Percentage indicates fraction of luminosity attributable to AGN activity for each line.

Resolution	Native (169 pc pix^{-1})	NGC 1365 330 pc pix^{-1}	500 pc pix^{-1}	1 kpc pix^{-1}
H α	4.85 ± 0.07 per cent	5.43 ± 0.06 per cent	5.75 ± 0.06 per cent	6.34 ± 0.05 per cent
H β	4.41 ± 0.27 per cent	4.86 ± 0.26 per cent	5.09 ± 0.24 per cent	5.54 ± 0.20 per cent
[O II]$\lambda\lambda$3726,3729	4.78 ± 1.76 per cent	5.23 ± 1.13 per cent	5.60 ± 1.02 per cent	6.35 ± 0.81 per cent
[O III]λ5007	10.06 ± 0.71 per cent	11.96 ± 0.72 per cent	12.35 ± 0.66 per cent	13.25 ± 0.52 per cent
[S II]$\lambda\lambda$6716,6731	5.65 ± 0.30 per cent	6.47 ± 0.28 per cent	6.97 ± 0.26 per cent	7.93 ± 0.21 per cent
[N II]λ6584	6.95 ± 0.20 per cent	8.49 ± 0.20 per cent	9.17 ± 0.18 per cent	10.32 ± 0.15 per cent
		NGC 1068		
Resolution	Native (121 pc pix^{-1})	330 pc pix^{-1}	500 pc pix^{-1}	1 kpc pix^{-1}
H α	25.23 ± 0.13 per cent	39.40 ± 0.10 per cent	39.07 ± 0.08 per cent	39.82 ± 0.05 per cent
H β	26.40 ± 0.81 per cent	38.91 ± 0.51 per cent	39.26 ± 0.38 per cent	42.31 ± 0.25 per cent
[O II]$\lambda\lambda$3726,3729	32.23 ± 6.81 per cent	25.27 ± 2.50 per cent	31.56 ± 2.18 per cent	42.68 ± 1.54 per cent
[O III]λ5007	42.69 ± 0.28 per cent	68.19 ± 0.16 per cent	68.75 ± 0.12 per cent	68.88 ± 0.07 per cent
[S II]$\lambda\lambda$6716,6731	33.38 ± 0.79 per cent	43.32 ± 0.43 per cent	44.15 ± 0.38 per cent	46.16 ± 0.21 per cent
[N II]λ6584	41.52 ± 0.31 per cent	64.58 ± 0.15 per cent	66.02 ± 0.11 per cent	67.62 ± 0.07 per cent

excited emission lines, with its high flux of [O III] very well documented (Phillips et al. 1983; Veilleux et al. 2003). Large [O III]/H β ratios in the nucleus of NGC 1365 (Phillips et al. 1983), as well as [O III]/H α ratios much larger than unity in the nucleus (Veilleux et al. 2003), have led previous authors to conclude the [O III] is produced by photoionization from the central AGN of NGC 1365.

Our results of starburst–AGN mixing are in agreement with the AGN activity in the nucleus of NGC 1365. Seen in Figs 12 and11 is the BPT diagram for NGC 1365, showcasing our new AGN fraction calculation. We note the presence of spaxels found below the 100 per cent star formation lines, and spaxels found above the 100 per cent AGN line. This indicates the uncertainties found within the photoionization models, and may arise due to systematic uncertainties in the input ionizing spectrum parameters (see D'Agostino et al. in preparation, for a detailed discussion on the systematic uncertainties in input ionizing stellar spectrum parameters in H II region modelling). Nevertheless, all spaxels which lie below the 100 per cent star formation lines are set to 100 per cent star formation, and all spaxels found above the 100 per cent AGN line are set to 100 per cent AGN. The map of the distribution of AGN fractions in NGC 1365 is shown in Fig. 13(a). Seen in Fig. 13(b) is the nucleus of NGC 1365, coloured by AGN fraction. The nucleus of NGC 1365 shows regions of high AGN activity, corresponding to high [O III]/H β and [N II]/H α emission line ratios. However, regions of high star formation (low AGN fractions) are also seen in the nucleus, with a clean mixing evident between regions of low and high AGN fractions. Star formation in the nucleus of NGC 1365 is also confirmed in the BPT diagram of NGC 1365 coloured by radius from the centre of the galaxy, shown in Fig. 9. Nuclear star formation in NGC 1365 has also been found previously (e.g. Phillips et al. 1983; Forbes & Norris 1998; Galliano et al. 2008; Alonso-Herrero et al. 2012, and references therein). In Fig. 13(b), we show the position of several star-forming clusters shown in Alonso-Herrero et al. (2012), coinciding with regions of low AGN fractions (high star-forming emission) in the nucleus of NGC 1365. Contours of 70 μm IR emission are also shown in Fig. 13(b), taken from Alexander & Hickox (2012). The detection of mid-IR emission at 70 μm (and other wavelengths; see Alexander & Hickox 2012) in the nucleus of NGC 1365 suggests an indirect detection of nuclear star formation, as a prominent dust lane surrounds the nuclear region of NGC 1365, obscuring a significant fraction of optical emission from our field of view (Alexander & Hickox 2012).

AGN activity south-east of the nucleus matches the biconical outflow seen in Veilleux et al. (2003), supporting the claim made by Veilleux et al. (2003) that the outflowing material is the result of AGN activity. Very little AGN activity, and in general structure, is seen on the north-west side of the nucleus. However, the north-west component of the [O III] biconical outflow is fainter than its south-east counterpart (Fig. 3 and Veilleux et al. 2003).

As a source of ionization and excitation, the AGN of NGC 1365 is relatively weak. This can be seen when considering the fraction of strong collisionally excited emission line fluxes as a result of AGN activity, as the fluxes of collisionally excited emission lines such as [O III] and [N II] are greatly enhanced by the extremely hard radiation field from the accretion disc of an AGN (Kewley et al. 2006, 2013). We measure the fraction of [O III] luminosity from AGN activity in NGC 1365 within the TYPHOON field of view to be 10.02 ± 0.71 per cent. Conversely, this implies that ∼90 per cent of the total [O III] luminosity in NGC 1365 within the TYPHOON field of view is from star formation, showing that star formation is the dominant process in NGC 1365. This is supported by the BPT diagram in Fig. 9, which not only shows an extensive star-forming sequence, but also shows star formation occurring in the nucleus of NGC 1365 along with AGN activity. Further, we calculate the radius at which star formation and AGN activity dominate equally (AGN fraction = 50 per cent) for NGC 1365 to be 1.350 ± 0.362 kpc. This calculation shows the majority of the AGN activity to be contained tightly within the nucleus with a very small radius of influence.

We calculate the fraction of the total H α luminosity attributable to AGN activity in NGC 1365 within the TYPHOON field of view to be 5.12 ± 0.07 per cent. As noted in Davies et al. (2014a), the AGN fractions in galaxies which display both processes indicate the degree of error imposed when using H α as a star formation rate (SFR) indicator. In the case of NGC 1365, SFRs calculated for NGC 1365 using H α can be considered largely accurate, as we observe ∼95 per cent of the total H α luminosity to be from star formation. At most, an overestimate of ∼5 per cent is expected when calculating SFRs in NGC 1365.

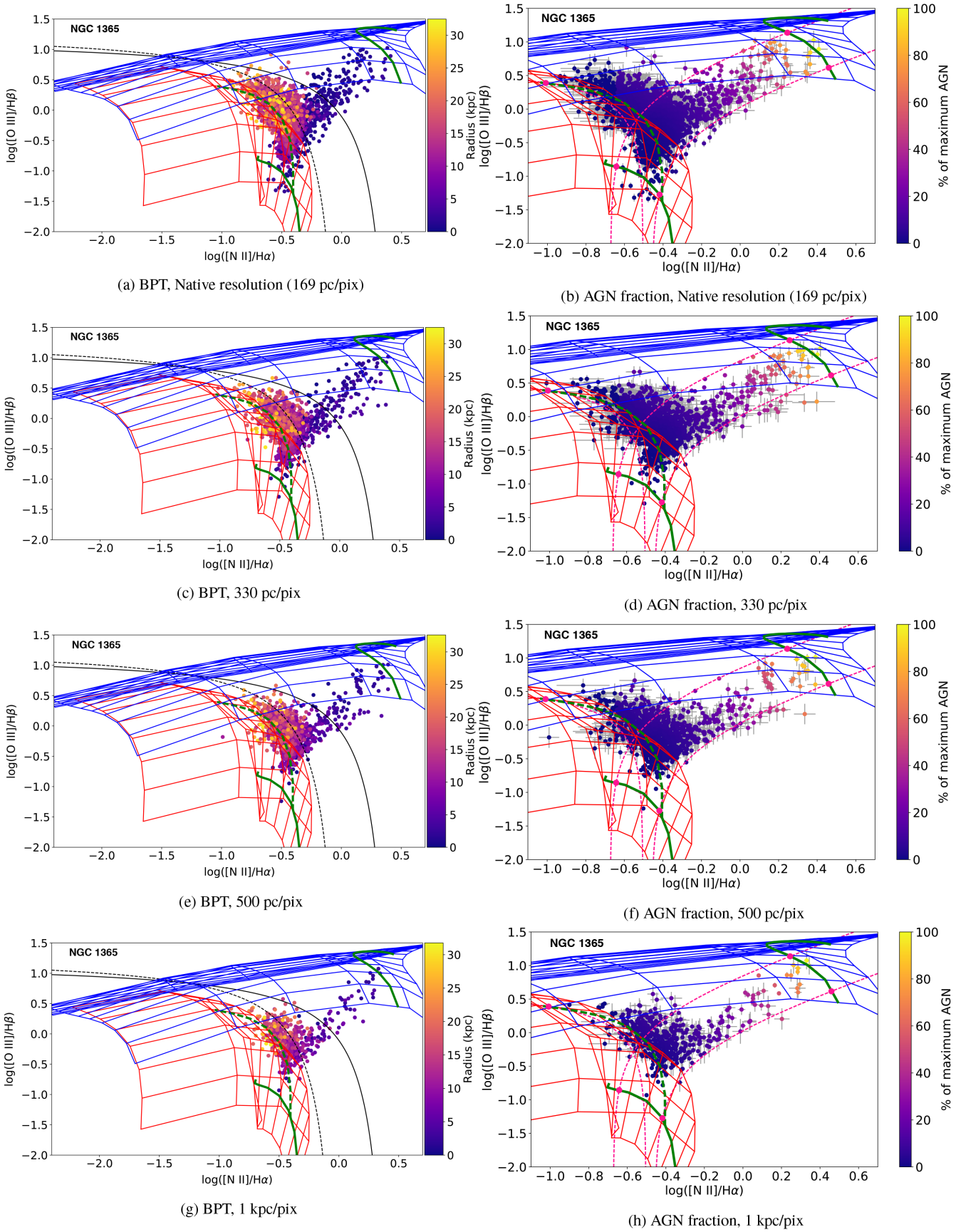

(a) BPT, Native resolution (169 pc/pix)

(b) AGN fraction, Native resolution (169 pc/pix)

(c) BPT, 330 pc/pix

(d) AGN fraction, 330 pc/pix

(e) BPT, 500 pc/pix

(f) AGN fraction, 500 pc/pix

(g) BPT, 1 kpc/pix

(h) AGN fraction, 1 kpc/pix

Figure 17. The AGN fractions and BPT diagrams coloured by radius for NGC 1365, after rebinning to lower spatial resolutions. Errors for the spaxels on the BPT diagrams are the same as those on the AGN fraction plots.

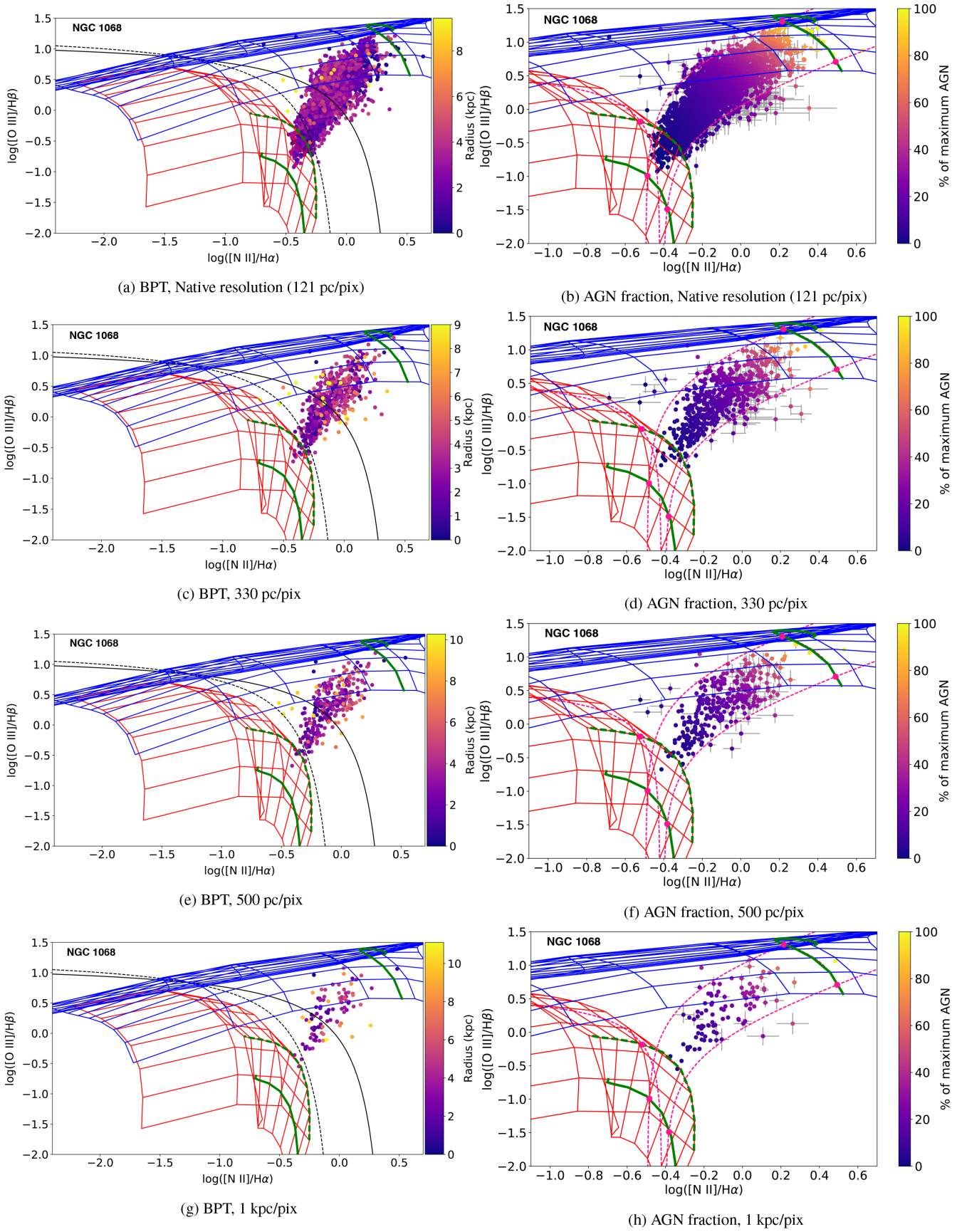

(a) BPT, Native resolution (121 pc/pix)

(b) AGN fraction, Native resolution (121 pc/pix)

(c) BPT, 330 pc/pix

(d) AGN fraction, 330 pc/pix

(e) BPT, 500 pc/pix

(f) AGN fraction, 500 pc/pix

(g) BPT, 1 kpc/pix

(h) AGN fraction, 1 kpc/pix

Figure 18. The AGN fractions and BPT diagrams coloured by radius for NGC 1068, after rebinning to lower spatial resolutions. Errors for the spaxels on the BPT diagrams are the same as those on the AGN fraction plots.

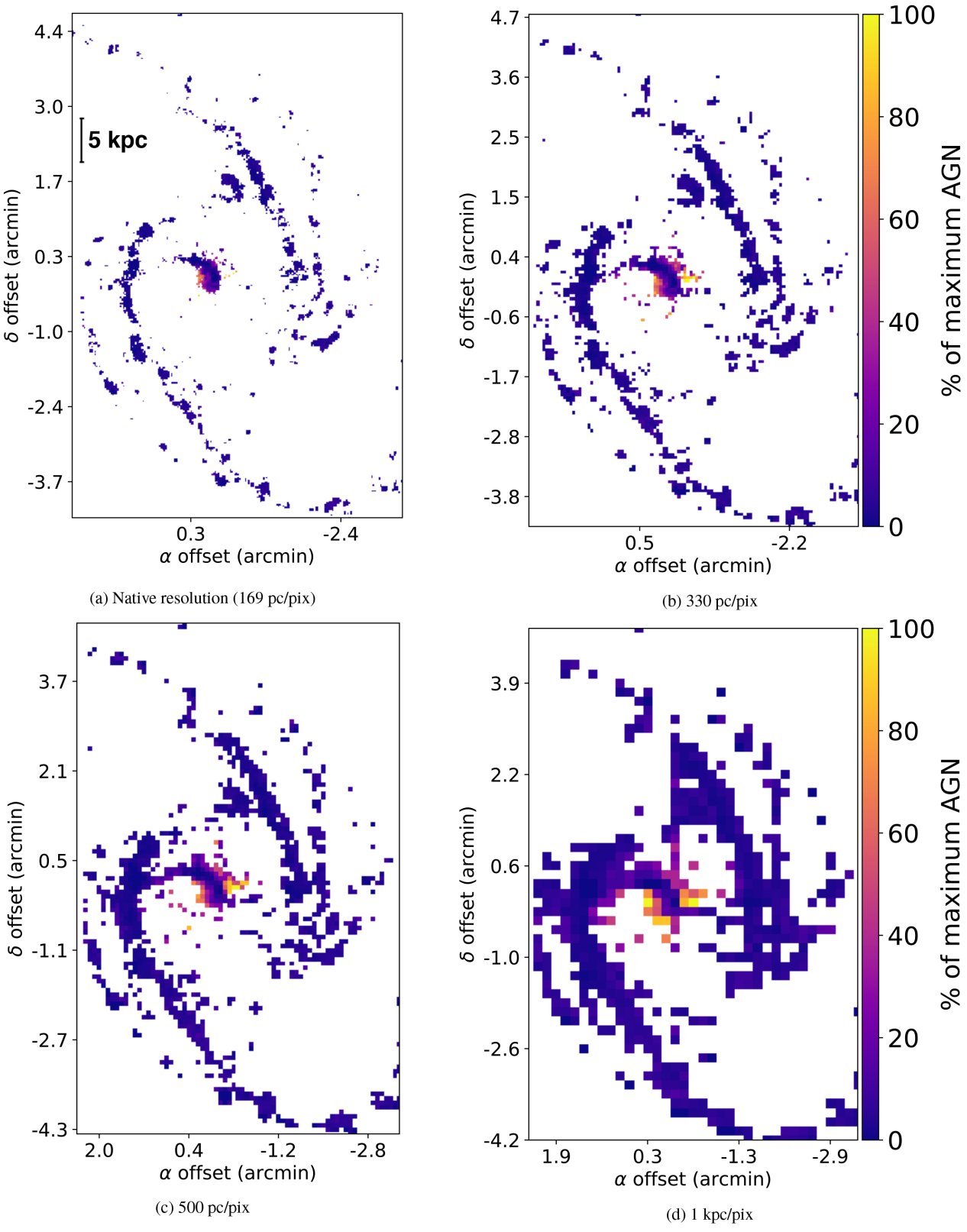

(a) Native resolution (169 pc/pix)

(b) 330 pc/pix

(c) 500 pc/pix

(d) 1 kpc/pix

Figure 19. The [O III]/H β versus [N II]/H α AGN fraction map for NGC 1365, after rebinning to lower spatial resolutions.

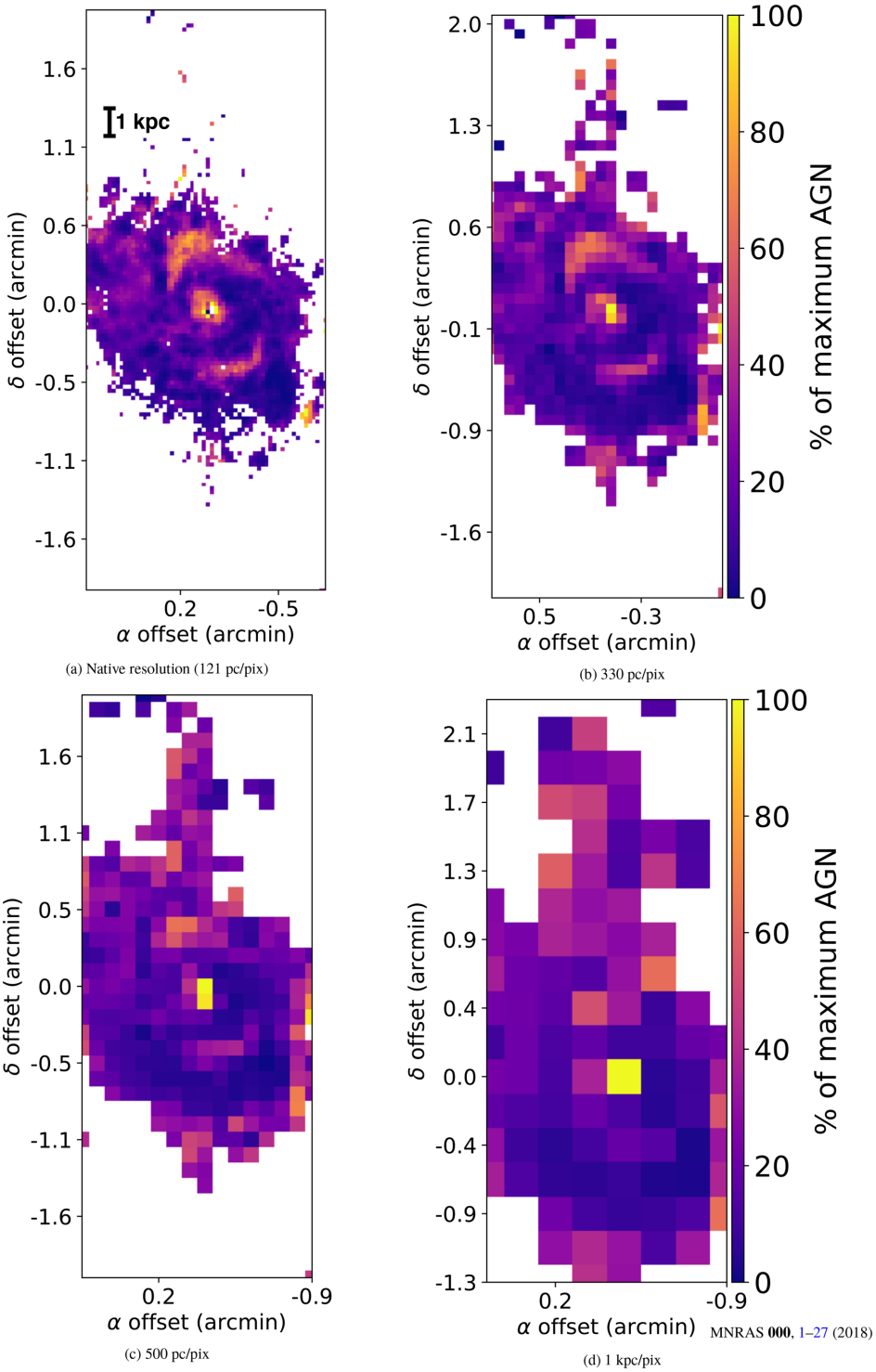

Figure 20. The [O III]/H β versus [N II]/H α AGN fraction map for NGC 1068, after rebinning to lower spatial resolutions.

5.4.2 NGC 1068

Figs 14 and 15 show the BPT diagram and subsequent AGN fraction calculation for NGC 1068. The map of the AGN fraction for NGC 1068 is shown in Fig. 16. Our findings support the claims made by Cecil et al. (2002) and Dopita et al. (2002b) regarding the driving force behind the large-scale outflows seen in NGC 1068. Material with a very high AGN fraction is seen in Fig. 16(a) to both the north-east of the galaxy, and to the south-west through openings in the galactic disc, coinciding with the biconical structure shown in Das et al. (2006). This suggests that the large-scale outflowing plume of [O III] seen in Pogge (1988) is the result of AGN-driven activity (shown in Fig. 16a).

AGN-driven outflow from NGC 1068 has also been concluded from results in radio wavelengths. Using data from ALMA, García-Burillo et al. (2014) map emission from a set of dense molecular

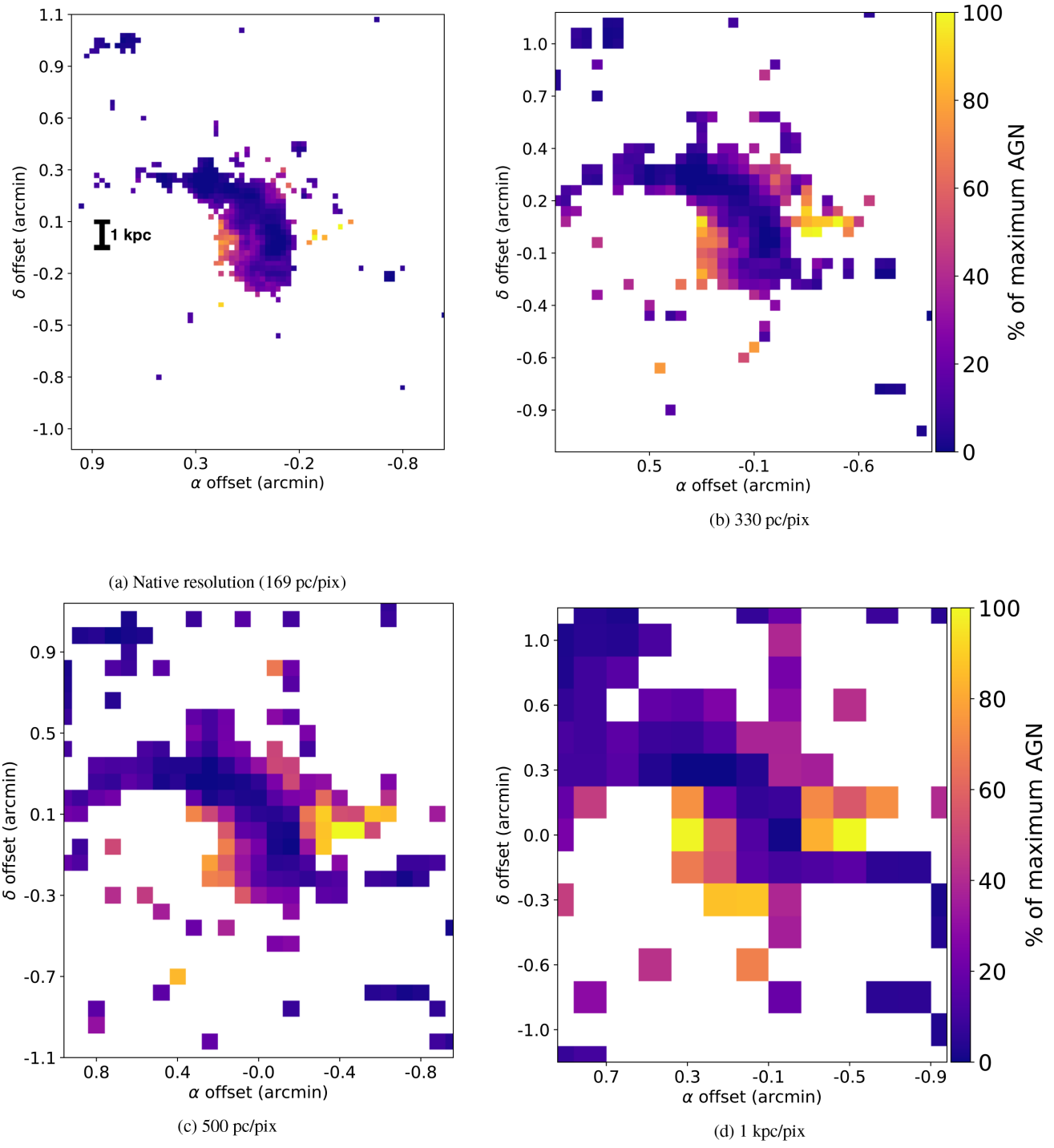

(a) Native resolution (169 pc/pix)

(b) 330 pc/pix

(c) 500 pc/pix

(d) 1 kpc/pix

Figure 21. Images from Fig. 19 with a zoom on the nuclear region of NGC 1365.

gas tracers, namely CO(3-2), CO(6-5), HCN(4-3), HCO^+ (4-3), and CS(7-6). Within the inner 50–400 pc, they report a massive outflow in all molecular gas tracers of $M_{\rm mol} = 2.7^{+0.9}_{-1.2} \times 10^7\,{\rm M}_\odot$. They also show a tight correlation between the ionized gas outflow, the radio jet, and outward motions within the circumnuclear disc of NGC 1068, suggesting the outflow is AGN-driven. They strengthen this suggestion by noting the outflow rate in the circumnuclear disc is $63^{+21}_{-37}\,{\rm M}_\odot\ {\rm yr}^{-1}$, much larger than the SFR calculated for NGC 1068 at these radii.

Star formation within the nucleus of NGC 1068 has been seen previously, with Storchi-Bergmann et al. (2012) locating young stars within the central 100 pc. The nuclear SFR in NGC 1068 is quite modest however, with estimates of $\rm SFR_{nuclear} \sim 0.4$–$0.7\,{\rm M}_\odot\ {\rm yr}^{-1}$ out to a radius of 35 pc (Davies et al. 2007), $\rm SFR_{nuclear} \sim 0.4\,{\rm M}_\odot\ {\rm yr}^{-1}$ out to a radius of 12 pc (Esquej et al. 2014), and $\rm SFR_{nuclear} \sim 1\,{\rm M}_\odot\ {\rm yr}^{-1}$ out to a radius of 140 pc.

Further out from the nucleus, up to radii of a few kpc, the SFR in NGC 1068 has been shown to be enormous. Thronson et al. (1989)

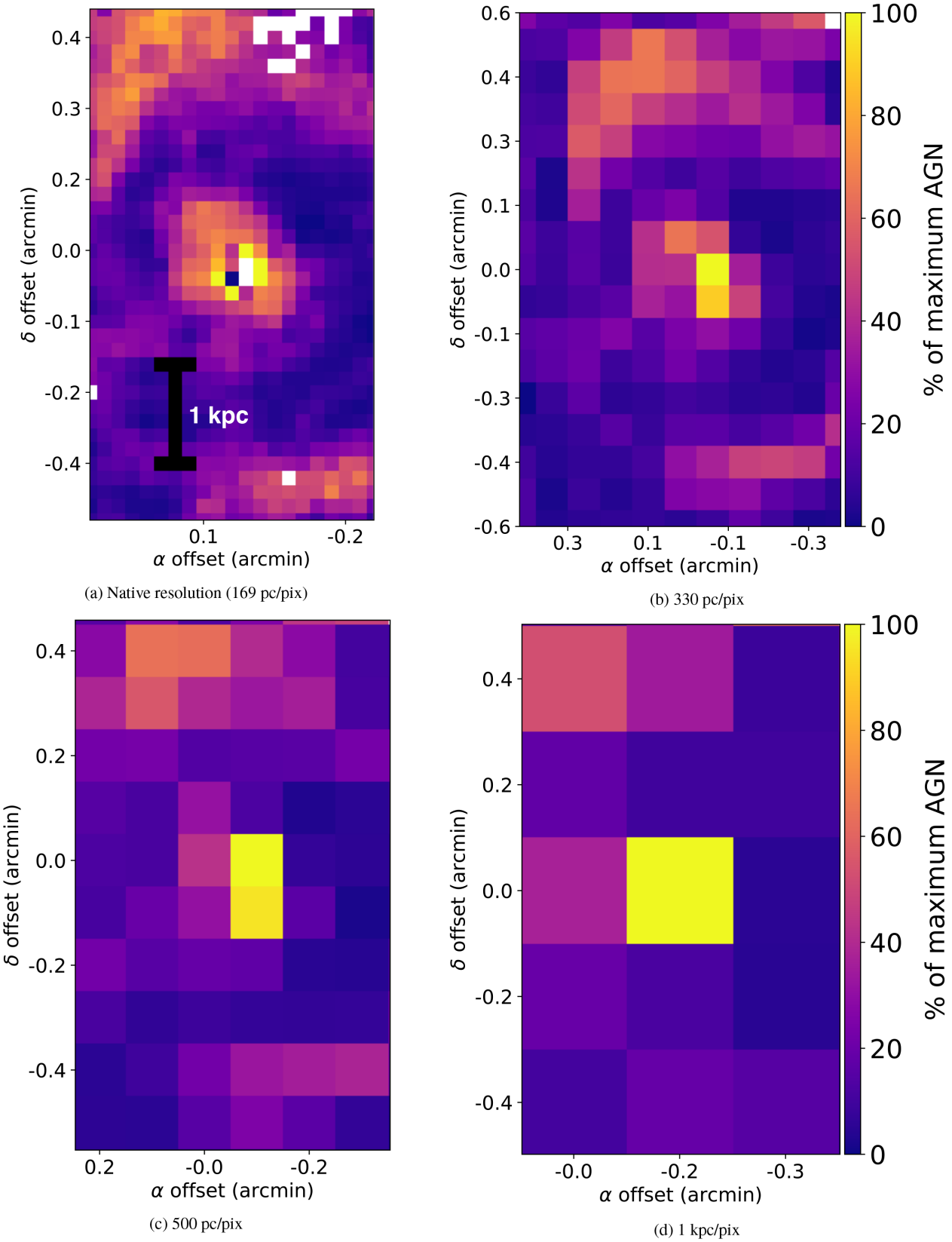

(a) Native resolution (169 pc/pix)

(b) 330 pc/pix

(c) 500 pc/pix

(d) 1 kpc/pix

Figure 22. Images from Fig. 20 with a zoom on the nuclear region of NGC 1068.

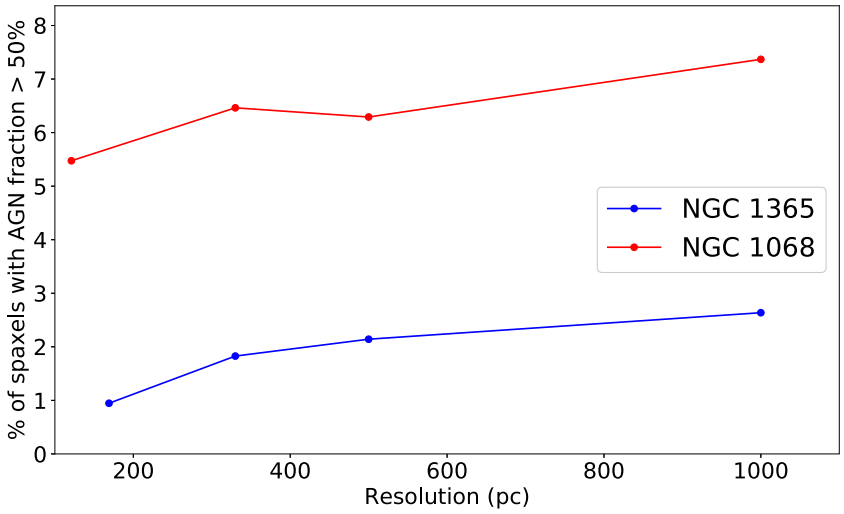

Figure 23. The percentage of spaxels in the BPTs of both NGC 1365 and NGC 1068 with AGN fractions of greater than 50 per cent as a function of spatial resolution. The four markers indicate (in order): native resolution (169 pc and 121 pc for NGC 1365 and NGC 1068, respectively), 330 pc, 500 pc, and 1000 pc (1 kpc).

calculate an SFR of $\sim$100 $M_\odot$ yr^{-1} in the ring surrounding the circumnuclear disc. The starburst ring in NGC 1068 can be seen in our results in Fig. 16(b) as a ring of spaxels with low AGN fraction surrounding the central region containing high AGN fractions. This large SFR is likely a consequence of the very large molecular mass in the circumnuclear region ($\sim$2–6 $\times$ 10^9 $M_\odot$), which appears to have been confined to the circumnuclear region by the bar at the centre of NGC 1068. As a result, star formation in NGC 1068 is seen to primarily take place in the star-forming ring surrounding the galaxy's central region. Hence, observations showing extensive star formation towards the outermost regions of NGC 1068 have been rare. This finding is reflected in the BPT diagram of NGC 1068 shown in Fig. 14 which lacks a large star-forming sequence like that seen in Fig. 12 for NGC 1365. Our results suggest that star formation as a source of ionization and excitation weakens at radii $\leq$2.246 $\pm$ 1.277 kpc, as these radii contain spaxels with AGN fractions greater than 50 per cent.

We show star formation nevertheless is influential in the total emission from NGC 1068, despite the lack of a star-forming sequence and a relatively low nuclear SFR. Presumably a result of the enormous SFR surrounding the circumnuclear disc, we calculate roughly $\sim$59 per cent of the total [O III] luminosity to be from star formation within the TYPHOON field of view (shown as an AGN fraction of 41.68 $\pm$ 0.28 per cent in Table 3). Our calculations in Table 3 also show star formation to be the dominant process in the emission of all collisionally excited lines considered within the TYPHOON field of view, with between $\sim$60–70 per cent of the total luminosity in the lines [O III]λ5007 ($\sim$58 per cent), [O II]$\lambda\lambda$3726,3729 ($\sim$68 per cent), [S II]$\lambda\lambda$6716, 6731($\sim$ 67 per cent), and [N II]λ6854 ($\sim$59 per cent) attributable to star formation rather than AGN emission.

We claim the use of the total Hα luminosity as an SFR indicator in NGC 1068 will overestimate the SFR by $\sim$25 per cent. Shown in Table 3, the luminosity of Hα from AGN activity is calculated to be 24.38 $\pm$ 0.12 per cent, implying only $\sim$75 per cent of the luminosity from Hα in NGC 1068 is from star formation.

6 INVESTIGATING THE EFFECT OF SPATIAL RESOLUTION

We investigate the AGN fraction and other properties as a function of spatial resolution. We apply the same calculations and methods described in Section 5 to data cubes rebinned to 330, 500, and 1000 pc pixel^{-1}; resolutions found in other IFU surveys such as MaNGA (Bundy et al. 2015), SAMI (Bryant et al. 2015), and CALIFA.

6.1 Effect of resolution on the AGN fraction

The AGN fraction calculations for NGC 1365 and NGC 1068 at differing resolutions are shown in Figs 17 and 18 as the BPT diagrams and in Figs 19 and 20 as maps of the galaxies. Figs 21 and 22 show maps of the AGN fraction in the nuclear regions of NGC 1365 and NGC 1068, respectively.

The basis point positions remain the same across all rebinned data for consistency, set to the values shown in Table 1. However, we do note following the work of Poetrodjojo et al. (), the metallicity gradient of a galaxy flattens with coarser resolution. Hence, if the metallicity gradient for both galaxies was recalculated using the rebinned data, the estimate for the central and outer metallicities would differ for each data cube, resulting in different positions for the basis points. We avoid this issue by noting the basis points are intended to represent line ratios associated with 100 per cent star formation and 100 per cent AGN emission. Binning together spaxels of AGN and star formation combines the processes in these spaxels, raising the overall contribution from AGN activity in the star-forming spaxels, and vice versa. The result is a diminishing spread of spaxels on the BPT diagram with coarser resolution. Hence, as the resolution coarsens, the likelihood of a spaxel containing 100 per cent emission from AGN activity or 100 per cent emission from star formation continues to decrease. This spread of spaxels on the BPT diagram is highest with the native resolution of both galaxies, suggesting the best indication of 100 per cent AGN emission and 100 per cent star-forming emission is provided by the

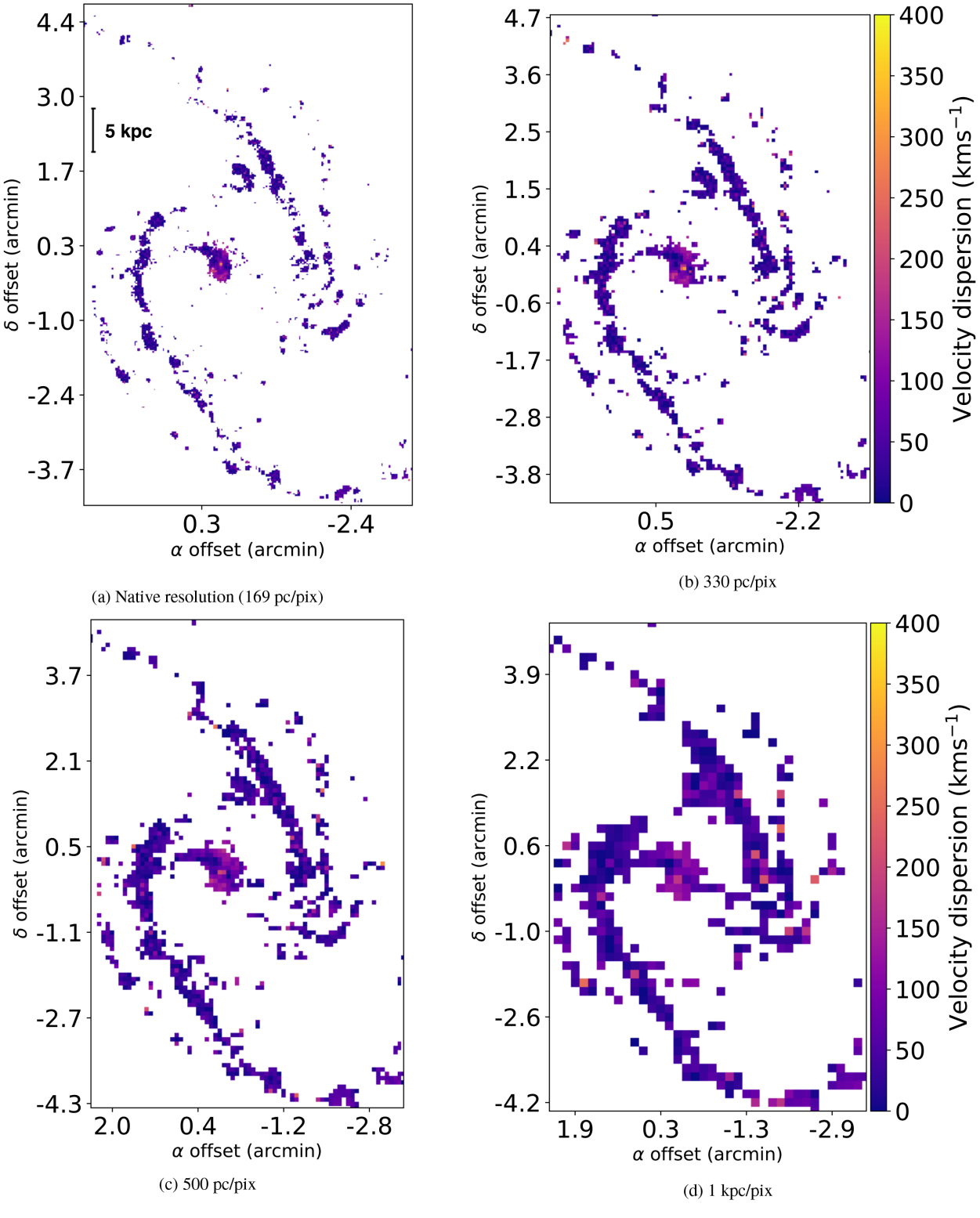

(a) Native resolution (169 pc/pix)

(b) 330 pc/pix

(c) 500 pc/pix

(d) 1 kpc/pix

Figure 24. The velocity dispersion maps for NGC 1365, after rebinning to lower resolutions.

highest resolution data cubes available.

The increase in AGN contribution in spaxels as the data are rebinned is shown in Table 2 which gives a constant increase in the radius of equal starburst–AGN domination for both galaxies (the radius where the AGN fraction = 50 per cent). It is also shown in Fig. 23, showing an average increase in the percentage of spaxels with AGN fractions >50 per cent as resolution decreases. The AGN radiation field produces large [O III] and [N II] line strengths, which dominate over the weaker line strengths from star formation, even at low AGN fractions.

In general, the AGN fractions for several strong emission lines (Hα, Hβ, [O II]$\lambda\lambda$3726,3729, [O III]λ5007, [S II]$\lambda\lambda$6716,6731, and

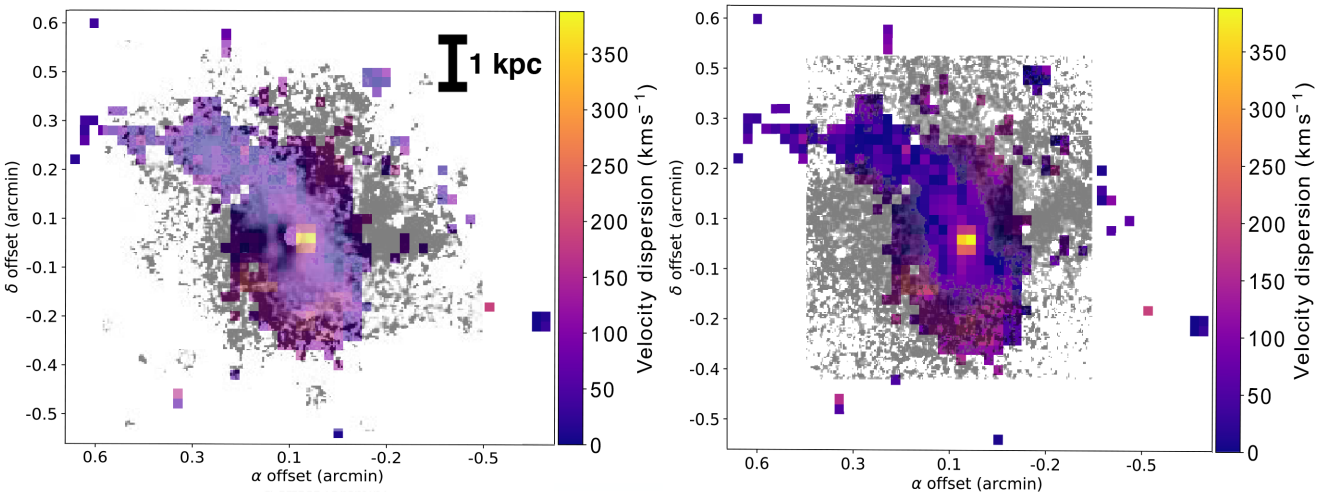

(a) [O III]/Hβ (b) [N II]/Hα

Figure 25. Outflows in [O III]/H β (a) and [N II]/H α (b) seen in the nucleus of NGC 1365 from Veilleux et al. (2003), coinciding with regions of high velocity dispersion. The [O III]/H β values in (a) range from 0 at the lightest to 3 at the darkest. The [N II]/H α values in (b) range from 0 at the lightest to 1.5 at the darkest.

[N II]λ6584) may increase with coarser resolution (Table 3). Considering NGC 1365, we find no significant change in the AGN fractions within the error bounds of the aforementioned strong emission lines between native resolution and a resolution of 1 kpc pix^{-1}, averaged over all lines shown in Table 3. NGC 1068, however, shows an average increase of 17.67 $\pm$ 7.09 per cent in the AGN fractions for the same strong emission lines between native resolution and a resolution of 1 kpc pix^{-1}. This has large ramifications for calculating the SFR in a galaxy. NGC 1068 shows an increase in the H α AGN fraction between native (121 pc pix^{-1}) and 1 kpc pix^{-1} resolutions of 14.59 $\pm$ 0.14 per cent. As a result, in general, the SFR from a galaxy with AGN activity may be continually and further overestimated with coarser spatial resolution.

We find that there is no limiting spatial resolution which allows the AGN fraction to be reliably estimated. The radius of equal starburst–AGN domination continues to decrease as the resolution increases (seen in Table 2), as does the percentage of spaxels with AGN fraction greater than 50 per cent (seen in Fig. 23). As such, one can expect the measurable emission from AGN to continue to decrease once the resolution has increased beyond the resolutions of the TYPHOON galaxies (169 pc pixel^{-1} for NGC 1365; 121 pc pixel^{-1} for NGC 1068). Hence, when attempting to accurately measure and quantify the influence and emission from an AGN, one should obtain data at a resolution as high as possible.

6.2 Effect of resolution on low surface brightness features

As the resolution decreases, low surface brightness (LSB) features become apparent. Seen in the BPT diagrams at lower resolutions are spaxels in the regions commonly associated with features such as shocks (for the position of shock features on diagnostic diagrams, see Rich et al. 2010; Rich, Kewley & Dopita 2011; Kewley et al. 2013). These LSB features typically have low signal-to-noise ratio values. The rebinning process produces an increase in the S/N of the LSB spaxels. Hence, LSB features become observable in the data. Table 2 shows the relative difference in spaxels with emission attributable to LSB features. In total, we see an increase in the percentage of spaxels which we attribute to low surface brightness features between the native resolution data and the rebinned data for both NGC 1365 and NGC 1068. The increase in the relative amount of spaxels attributed to LSB features differs for both galaxies, with up to a factor of $\sim$12.5 increase in NGC 1365 with coarser resolution, and up to a factor of $\sim$1.6 increase in NGC 1068. These spaxels are defined as being outside the nuclear column with moderate [O III]/H β and moderate-high [N II]/H α ratios, in the region of the BPT where LSB features are typically found.

6.2.1 *Shocks*

Shocks (or shock waves) are compression waves which propagate at a speed greater than the sound speed in the medium. Due to the supersonic nature of the shock wave, instantaneous changes in properties of the medium (such as density, pressure, and temperature) occur at the shock front, causing discontinuities in the values of these properties before and after the boundary of the shock. The source of supersonic compression may originate from astrophysical phenomena such as supernova explosions, stellar winds, or outflows from young stellar clusters or AGNs (Dopita & Sutherland 2003, and references therein).

Shocks are typically diagnosed and categorized by their high velocity dispersions (typically $\sim$100–500 km s^{-1}; Rich et al. 2010, 2011; Ho et al. 2014; Rich, Kewley & Dopita 2014). Fig. 24 shows the velocity dispersion maps across all resolutions considered for NGC 1365. Regions of high velocity dispersion ($\sigma \sim 160$ km s^{-1}) can be seen around the nucleus of NGC 1365 across all resolutions. However, the high velocity dispersion regions surrounding the nucleus grow in size as resolution decreases. The high-σ areas surrounding the nucleus are aligned with the biconical outflow in [N II]/H α and [O III]/H β shown in NGC 1365 from Veilleux et al. (2003) (shown in Fig. 25), suggesting the shocks in NGC 1365 are the result of outflow from the central AGN.

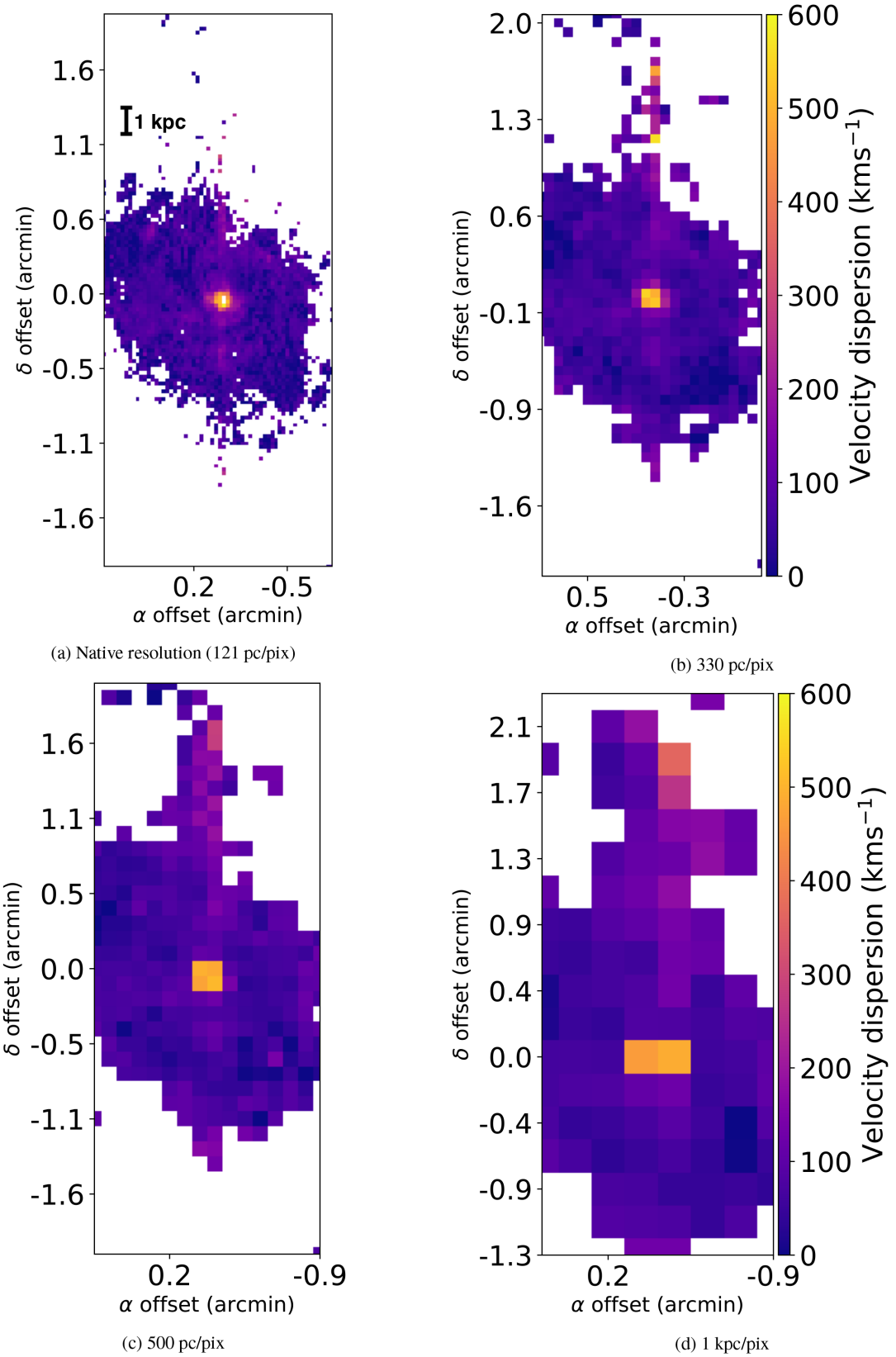

(a) Native resolution (121 pc/pix)

(b) 330 pc/pix

(c) 500 pc/pix

(d) 1 kpc/pix

Figure 26. The velocity dispersion maps for NGC 1068, after rebinning to lower resolutions.

The number of regions of high velocity dispersion along the spiral arms of NGC 1365 increases as the resolution decreases, with velocity dispersions up to $\sigma \sim 300\,\mathrm{km\,s^{-1}}$ at a resolution of $1\,\mathrm{kpc\,pix^{-1}}$. The high levels of star formation in the spiral arms of NGC 1365 shown in Figs 12 and 13(a) suggest that regions of high velocity dispersion within the spiral arms are a result of shocks from stellar sources, such as supernova explosions and stellar winds. It appears that shocks from stellar sources are intensified and enhanced with coarser resolution.

NGC 1068 also shows evidence of shocks. Seen in the velocity dispersion maps for NGC 1068 in Fig. 26, regions of high velocity dispersion can be seen away from the central AGN, notably along the biconical outflowing material. An accreting SBH will produce thermal X-rays which provide a radiation pressure on nearby gas, causing expulsion of the gas in the form of a wind. The biconical outflow, believed to be the result of AGN activity (and our Fig. 16; Pogge 1988; Cecil et al. 2002; Dopita et al. 2002b), is radiatively accelerated to high velocities ($\sim$3000 km s^{-1} in the case of NGC 1068; Cecil et al. 2002) by the AGN wind. Once the wind enters the ISM, the high-velocity material interacts with the ISM material, which is travelling at a velocity of the order of the sound speed in the medium ($\sim$ a few tens of km s^{-1}; Dopita & Sutherland 2003). The high-velocity outflowing material, travelling at a velocity higher than the sound speed in the medium, compresses the ISM material upon interaction, causing shocks through the ISM (Zubovas & King 2012). Hence, it is expected that regions of high velocity dispersion which correspond to shocks appear within the biconical outflowing material found in NGC 1068. The number and relative amount of the high velocity dispersion regions along the biconical outflow continue to increase as the resolution decreases. The spaxels in the area concerning shocks on the BPT diagrams for NGC 1068 shown in Fig. 18 are assigned large radii ($r > 5$ kpc), constraining these spaxels to be outside the disc of NGC 1068.

7 CONCLUSIONS

Using high spatial resolution data from the TYPHOON/PrISM survey, we analyse two AGN host galaxies NGC 1365 and NGC 1068. We extend the work of Davies et al. (2014a,b) by using photoionization grids to introduce a new method to calculate the AGN fraction of a galaxy from the BPT diagram. We also perform the same AGN fraction calculations on data cubes of NGC 1365 and NGC 1068 which have been rebinned to lower spatial resolutions. We report the following:

(i) IFU data cubes with resolutions as high as those used by TYPHOON (169 pc pix^{-1} for NGC 1365; 121 pc pix^{-1} for NGC 1068) show both star formation and AGN activity occurring in the nucleus of an AGN host galaxy.

(ii) The AGN in NGC 1365 is relatively weak, with only $\sim$10 per cent of the total [O III]λ5007 luminosity and $\sim$5 per cent of the total Hα luminosity from NGC 1365 being attributable to AGN activity within the TYPHOON field of view. This shows that the vast majority of the emission from NGC 1365 is from star formation. The AGN in NGC 1068 is stronger, accounting for $\sim$42 per cent of the total [O III] luminosity and $\sim$24 per cent of the total Hα luminosity within the TYPHOON field of view. This shows that while AGN activity in NGC 1068 is considerable, star formation does have a large influence in the total emission from NGC 1068. The fraction of Hα emission from AGN activity also has consequences for the calculation of SFRs in both of these galaxies. An overestimate of $\sim$5 per cent and an overestimate of $\sim$24 per cent on the SFR of NGC 1365 and NGC 1068, respectively, will occur if Hα is used for the calculation.

(iii) Low surface brightness features such as shocks in galaxies and certain outflows (such as that in NGC 1365) only appear at lower resolutions. Features with a low S/N ratio gain an S/N increase when binned with spaxels containing a higher S/N ratio, or when observed with a higher S/N feature in the same spaxel. Increases in the number of spaxels attributable to low surface brightness features up to factors of $\sim$12.5 and $\sim$1.6 are noticed with coarser resolution in NGC 1365 and NGC 1068, respectively. Hence, certain features within a galaxy are lost when the resolution of the observations increases.

(iv) The contribution of an AGN to total galaxy emission increases with coarser resolution. An average 18.05 per cent increase in the emission from AGN activity in NGC 1068 is seen in several strong lines as the resolution decreases from their respective native resolutions to a resolution of $1\,\mathrm{kpc\,pix^{-1}}$. As the resolution lowers, the AGN fraction in individual spaxels and also individual emission lines increases, showing a larger effect from the AGN. This is also seen by the radius of equal starburst–AGN domination increasing with coarser resolution, with a roughly equal factor of 3 increase in the radius of equal domination for both NGC 1365 and NGC 1068 as the resolution decreases from their respective native resolutions to a resolution of $1\,\mathrm{kpc\,pix^{-1}}$.

For optimal results when calculating the contribution of emission from AGN activity, the highest possible resolution data should be sought. We show that with finer resolution, the relative contribution from an AGN in the total emission within the galaxy continuously decreases. Furthermore, the zone of influence of the AGN is also shown to be continually overestimated with coarser resolution. Hence, only the highest possible resolution will provide the most accurate measure of the AGN activity within a galaxy.

We intend to extend this project in the future. Emission in galaxies may arise from sources other than AGNs or star formation, such as shocks. Hence, future work will include the separation of emission from shocks in addition to AGN and star formation in IFU data.

ACKNOWLEDGEMENTS

Parts of this research were conducted by the Australian Research Council Centre of Excellence for All Sky Astrophysics in 3 Dimensions (ASTRO 3D), through project number CE170100013. The authors would also like to thank referee Santiago García-Burillo, who provided valuable input and helped improve the condition of the publication.

REFERENCES

Ackermann M. et al., 2011, ApJ, 743, 171
Alexander D. M., Hickox R. C., 2012, New Astron. Rev., 56, 93
Alloin D., Edmunds M. G., Lindblad P. O., Pagel B. E. J., 1981, A&A, 101, 377
Alonso-Herrero A. et al., 2012, MNRAS, 425, 311
Anders E., Grevesse N., 1989, Geochim. Cosmochim. Acta, 53, 197
Antonucci R. R. J., Miller J. S., 1985, ApJ, 297, 621
Armus L. et al., 2009, PASP, 121, 559
Arribas S., Mediavilla E., Garcia-Lorenzo B., 1996, ApJ, 463, 509
Baldwin J. A., Phillips M. M., Terlevich R., 1981, PASP, 93, 5
Belsole E., Worrall D. M., Hardcastle M. J., 2006, MNRAS, 366, 339
Bennert V. N., Auger M. W., Treu T., Woo J.-H., Malkan M. A., 2011, ApJ, 742, 107
Bryant J. J., et al., 2015, MNRAS, 447, 2857
Bundy K., et al., 2015, ApJ, 798, 7

Cattaneo A., Haehnelt M. G., Rees M. J., 1999, MNRAS, 308, 77
Cecil G., Bland J., Tully R. B., 1990, ApJ, 355, 70
Cecil G., Dopita M. A., Groves B., Wilson A. S., Ferruit P., Pécontal E., Binette L., 2002, ApJ, 568, 627
Charlot S., Longhetti M., 2001, MNRAS, 323, 887
Cid Fernandes R., Heckman T., Schmitt H., González Delgado R. M., Storchi-Bergmann T., 2001, ApJ, 558, 81
Crenshaw D. M., Kraemer S. B., 2000, ApJ, 532, L101
da Silva R. L., Fumagalli M., Krumholz M., 2012, ApJ, 745, 145
Das V., Crenshaw D. M., Kraemer S. B., Deo R. P., 2006, AJ, 132, 620
Davies R. I., Müller Sánchez F., Genzel R., Tacconi L. J., Hicks E. K. S., Friedrich S., Sternberg A., 2007, ApJ, 671, 1388
Davies R. L., Kewley L. J., Ho I.-T., Dopita M. A., 2014b, MNRAS, 444, 3961
Davies R. L., Rich J. A., Kewley L. J., Dopita M. A., 2014a, MNRAS, 439, 3835
de Vaucouleurs G., de Vaucouleurs A., Corwin H. G. Jr. Buta R. J., Paturel G., Fouqué P., 1991, Third Reference Catalogue of Bright Galaxies. Volume I: Explanations and references. Volume II: Data for galaxies between 0^h and 12^h. Volume III: Data for galaxies between 12^h and 24^h, Springer, New York, NY (USA).
Dopita M. A., Groves B. A., Sutherland R. S., Binette L., Cecil G., 2002b, ApJ, 572, 753
Dopita M. A., Pereira M., Kewley L. J., Capaccioli M., 2002a, ApJS, 143, 47
Dopita M. A., Sutherland R. S., 2003, Astrophysics of the Diffuse Universe, Springer, Berlin, New York
Esquej P. et al., 2014, ApJ, 780, 86
Evans I. N., Ford H. C., Kinney A. L., Antonucci R. R. J., Armus L., Caganoff S., 1991, ApJ, 369, L27
Feltre A., Charlot S., Gutkin J., 2016, MNRAS, 456, 3354
Ferrarese L., Merritt D., 2000, ApJ, 539, L9
Forbes D. A., Norris R. P., 1998, MNRAS, 300, 757
Galliano E., Alloin D., Pantin E., Granato G. L., Delva P., Silva L., Lagage P. O., Panuzzo P., 2008, A&A, 492, 3
Galliano E., Alloin D., Pantin E., Lagage P. O., Marco O., 2005, A&A, 438, 803
Gallimore J. F., Baum S. A., O'Dea C. P., Pedlar A., 1996, ApJ, 458, 136
García-Burillo S. et al., 2014, A&A, 567, A125
García-Burillo S. et al., 2016, ApJ, 823, L12
Gebhardt K. et al., 2000, ApJ, 539, L13
Goosmann R. W., Matt G., 2011, MNRAS, 415, 3119
Granato G. L., De Zotti G., Silva L., Bressan A., Danese L., 2004, ApJ, 600, 580
Groves B. A., Dopita M. A., Sutherland R. S., 2004, ApJS, 153, 9
Groves B. A., Heckman T. M., Kauffmann G., 2006, MNRAS, 371, 1559
Gültekin K. et al., 2009, ApJ, 698, 198
Haehnelt M. G., Kauffmann G., 2000, MNRAS, 318, L35
Hillier D. J., Miller D. L., 1998, ApJ, 496, 407
Hjelm M., Lindblad P. O., 1996, A&A, 305, 727
Ho I.-T., 2016, LZIFU: IDL Emission Line Fitting Pipeline for Integral Field Spectroscopy Data, Astrophysics Source Code Library, record ascl:1607.018
Ho I.-T. et al., 2014, MNRAS, 444, 3894
Ho I.-T. et al., 2016, Ap&SS, 361, 280
Ho I.-T. et al., 2017, ApJ, 846, 39
Husemann B. et al., 2013, A&A, 549, A87
Jenkins E. B., 2014, Proc. Sci., conference: Life Cycleof Dust in the Universe, Observations, Theory and Laboratory Experiments, preprint (arXiv:1402.4765)
Kauffmann G. et al., 2003, MNRAS, 346, 1055
Kewley L. J., Dopita M. A., Leitherer C., Davé R., Yuan T., Allen M., Groves B., Sutherland R., 2013, ApJ, 774, 100
Kewley L. J., Dopita M. A., Sutherland R. S., Heisler C. A., Trevena J., 2001, ApJ, 556, 121
Kewley L. J., Groves B., Kauffmann G., Heckman T., 2006, MNRAS, 372, 961
Kobulnicky H. A., Kewley L. J., 2004, ApJ, 617, 240
Kristen H., Jorsater S., Lindblad P. O., Boksenberg A., 1997, A&A, 328, 483
Kroupa P., 2002, Science, 295, 82
Krumholz M. R., Fumagalli M., da Silva R. L., Rendahl T., Parra J., 2015, MNRAS, 452, 1447
LaMassa S. M., Heckman T. M., Ptak A., Schiminovich D., O'Dowd M., Bertincourt B., 2012, ApJ, 758, 1
Lejeune T., Cuisinier F., Buser R., 1997, A&AS, 125
Magorrian J. et al., 1998, AJ, 115, 2285
Marconi A., Hunt L. K., 2003, ApJ, 589, L21
Marinucci A. et al., 2016, MNRAS, 456, L94
McConnell N. J., Ma C.-P., 2013, ApJ, 764, 184
Meynet G., Maeder A., Schaller G., Schaerer D., Charbonnel C., 1994, A&AS, 103
Miller J. S., Antonucci R. R. J., 1983, ApJ, 271, L7
Miller J. S., Goodrich R. W., Mathews W. G., 1991, ApJ, 378, 47
Morganti R., Tsvetanov Z. I., Gallimore J., Allen M. G., 1999, A&AS, 137, 457
Nicholls D. C., Sutherland R. S., Dopita M. A., Kewley L. J., Groves B. A., 2017, MNRAS, 466, 4403
Osterbrock D. E., Martel A., 1993, ApJ, 414, 552
Pauldrach A. W. A., Hoffmann T. L., Lennon M., 2001, A&A, 375, 161
Phillips M. M., Edmunds M. G., Pagel B. E. J., Turtle A. J., 1983, MNRAS, 203, 759
Pogge R. W., 1988, ApJ, 328, 519
Poncelet A., Sol H., Perrin G., 2008, A&A, 481, 305
Rafferty D. A., Brandt W. N., Alexander D. M., Xue Y. Q., Bauer F. E., Lehmer B. D., Luo B., Papovich C., 2011, ApJ, 742, 3
Reynolds C. S., 2013, Nature, 494, 432
Rich J. A., Dopita M. A., Kewley L. J., Rupke D. S. N., 2010, ApJ, 721, 505
Rich J. A., Kewley L. J., Dopita M. A., 2011, ApJ, 734, 87
Rich J. A., Kewley L. J., Dopita M. A., 2014, ApJ, 781, L12
Rigby J. R., 2006, PhD thesis, The University of Arizona
Risaliti G., Elvis M., Fabbiano G., Baldi A., Zezas A., Salvati M., 2007, ApJ, 659, L111
Risaliti G. et al., 2013, Nature, 494, 449
Sandqvist A., Joersaeter S., Lindblad P. O., 1995, A&A, 295, 585
Sandqvist A., Jorsater S., Lindblad P. O., 1982, A&A, 110, 336
Sharp R. G., Bland-Hawthorn J., 2010, ApJ, 711, 818
Storchi-Bergmann T., Riffel R. A., Riffel R., Diniz M. R., Borges Vale T., McGregor P. J., 2012, ApJ, 755, 87
Sturch L. K., Madore B. F., 2012, in Tuffs R. J., Popescu C. C., eds, IAU Symp. 284, The Spectral Energy Distribution of Galaxies - SED 2011. Kluwer, Dordrecht, p. 180
Sánchez S. F. et al., 2012, A&A, 538, A8
Thilker D. A., Braun R., Walterbos R. A. M., 2000, AJ, 120, 3070
Thronson H. A., Jr. et al., 1989, ApJ, 343, 158
Tremaine S. et al., 2002, ApJ, 574, 740
Veilleux S., Osterbrock D. E., 1987, ApJS, 63, 295
Veilleux S., Shopbell P. L., Rupke D. S., Bland-Hawthorn J., Cecil G., 2003, AJ, 126, 2185
Véron-Cetty M.-P., Véron P., 2006, A&A, 455, 773
Wilson A. S., Helfer T. T., Haniff C. A., Ward M. J., 1991, ApJ, 381, 79
Wilson A. S., Ulvestad J. S., 1983, ApJ, 275, 8
Wilson A. S., Ulvestad J. S., 1987, ApJ, 319, 105
Yuan T.-T., Kewley L. J., Sanders D. B., 2010a, ApJ, 709, 884
Yuan T.-T., Kewley L. J., Sanders D. B., 2010b, ApJ, 709, 884
Zubovas K., King A. R., 2012, in Chartas G., Hamann F., Leighly K. M., eds, ASP Conf. Ser. Vol. 460, AGN Winds in Charleston. Astron. Soc. Pac., San Francisco, p. 235

APPENDIX: POWER-LAW SPECTRAL INDEX

Here we show BPT diagrams of NGC 1365 and NGC 1068 in Figs. A1 and A2, respectively, with AGN model grids featuring power-law spectral indices of $\alpha = -1.4$ and -1.7. In both $n = 1000\,\mathrm{cm}^{-3}$ and $n = 10\,000\,\mathrm{cm}^{-3}$ cases for NGC 1365 and NGC 1068, re-

spectively, lowering the spectral index α lowers the [O III]/H β and [N II]/H α fluxes produced by the models. Several caveats result from using a lower spectral index with these models:

(i) The line of constant metallicity representing the central region of the galaxy is moved further down the mixing sequence towards the starburst region of the BPT diagram, and in the case of NGC 1068, does not provide a good fit to the uppermost spaxels in the mixing sequence. The result of using such a model to define the 100 per cent AGN region would be many spaxels saturated at 100 per cent AGN. Further, the error in the photoionization models of ∼1.5 dex in emission line ratio (D'Agostino et al. in preparation) does not account for the amount of spaxels above the central metallicity line.

(ii) While a case may be made for the use of $\alpha = -1.4$ for NGC 1365 seen in Fig. A1(a) on, use of such a model (and models which decrease α even further) results in several off-grid spaxels which are not explained or defined by the model. At $\alpha = -1.7$ and below, increasing the metallicity of the $n = 1000\,\mathrm{cm}^{-3}$ models fails to describe the off-grid spaxels, as the models begin to turn over at metallicities of $Z = 0.060$ and beyond, seen in Fig. A1(b) on. A turn in the shape of the model is not yet evident when using $\alpha =$

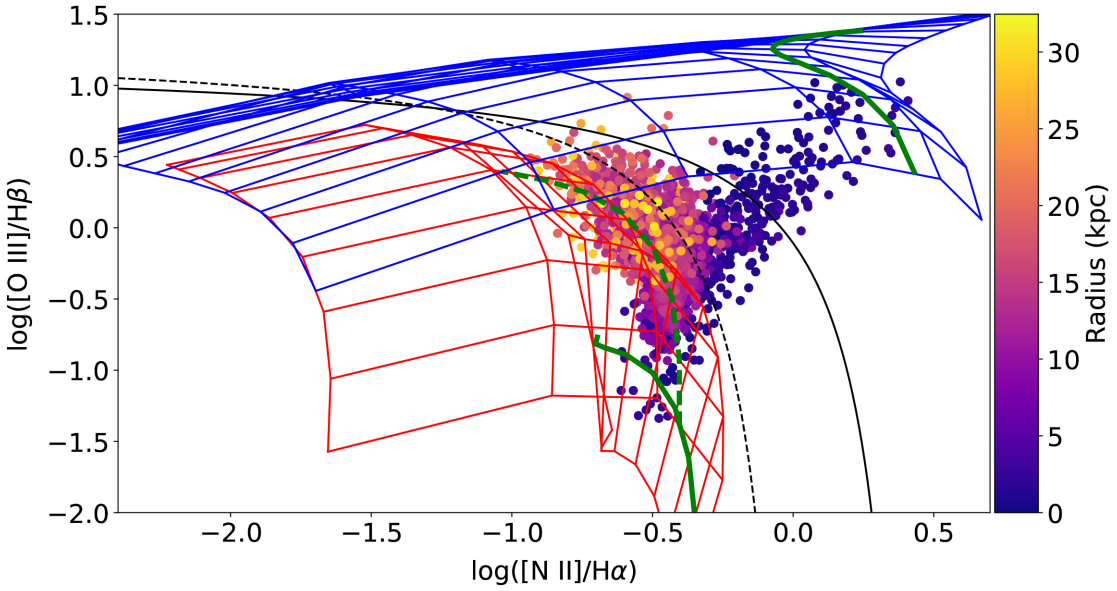

(a) $\alpha = -1.4$

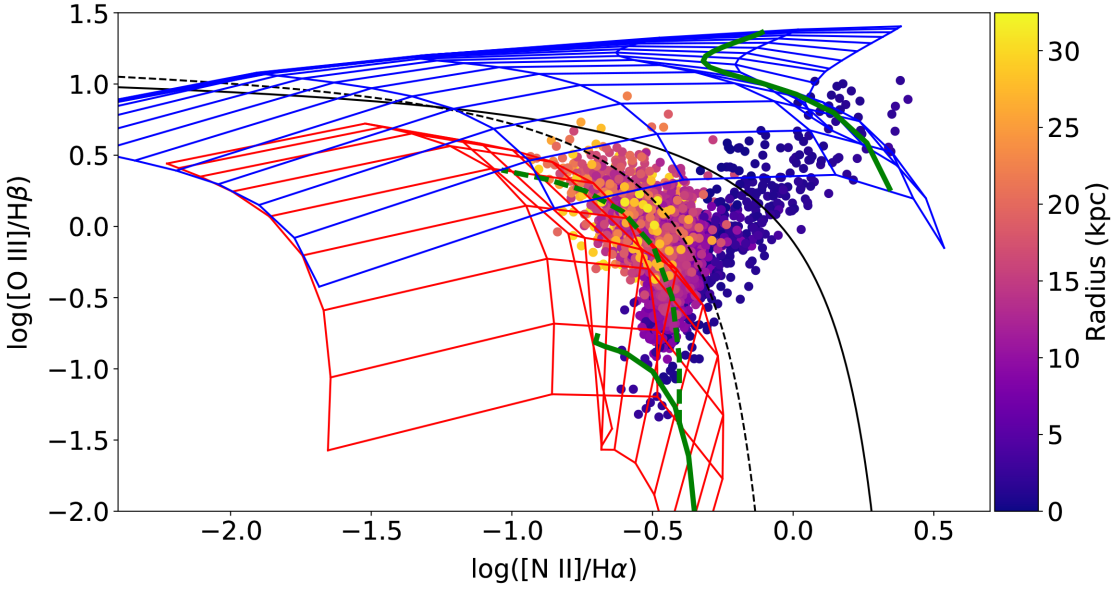

(b) $\alpha = -1.7$

Figure A1. NGC 1365, showing $n = 1000\,\mathrm{cm}^{-3}$ AGN model grids computed with power-law spectral indices of $\alpha = -1.4$ and -1.7.

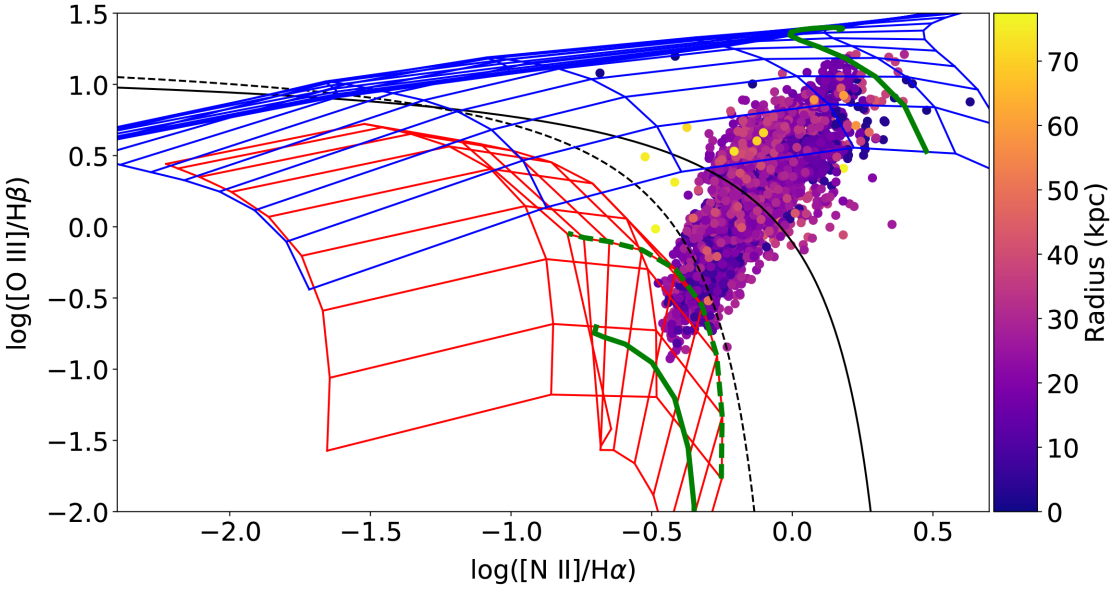

(a) $\alpha = -1.4$

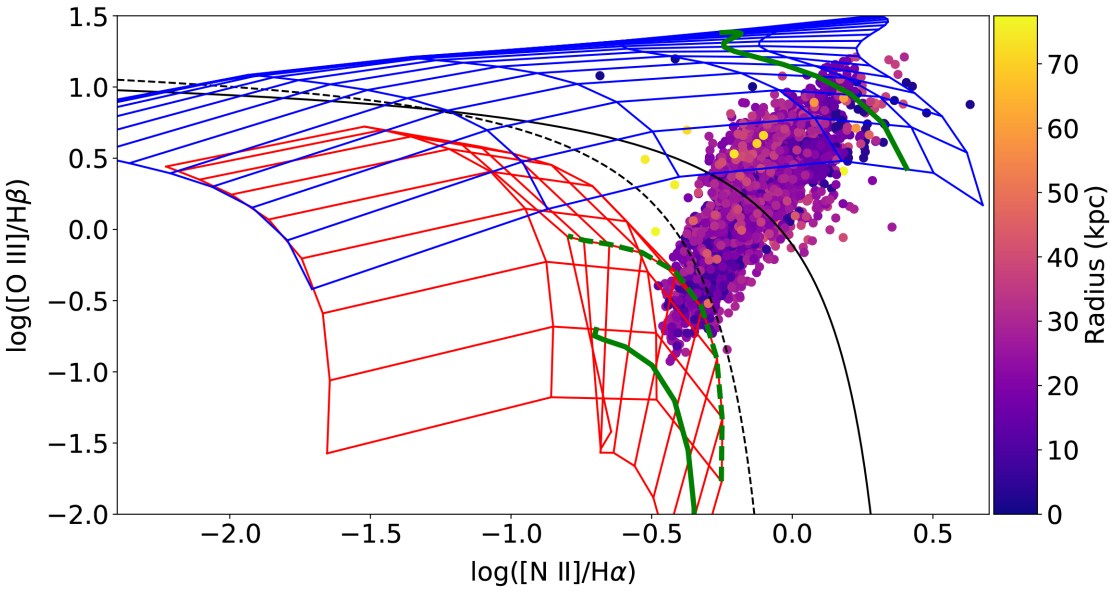

(b) $\alpha = -1.7$

Figure A2. NGC 1068, showing $n = 10\,000\,\mathrm{cm}^{-3}$ AGN model grids computed with power-law spectral indices of $\alpha = -1.4$ and -1.7.

-1.4 for the $n = 1000\,\mathrm{cm}^{-3}$ model seen in Fig. A1(a) on, hence increasing the maximum metallicity shown in the model beyond $Z = 0.060$ may describe the off-grid spaxels. However, it should be noted that the maximum metallicity calculated in each galaxy (1.42 and 1.41 $Z_\odot$ for NGC 1365 and NGC 1068, respectively, where $Z_\odot \equiv Z = 0.020$) is far below the maximum already included in the models of $Z = 0.060$. Hence, using higher metallicities to explain the off-grid spaxels is inconsistent with our metallicity calculations, and such a high metallicity is possibly considered unphysical.

Hence, a power-law spectral index of $\alpha = -1.2$ is the only value considered which is consistent with the data and our metallicity calculations.

This paper has been typeset from a TEX/LATEX file prepared by the author.